

THREE-PHOTON MICROSCOPY AT 1700 NM FOR *IN VIVO* IMAGING

A Dissertation

Presented to the Faculty of the Graduate School

of Cornell University

In Partial Fulfillment of the Requirements for the Degree of

Doctor of Philosophy

by

Nicholas Geoffrey Horton

May 2015

© 2015 Nicholas Geoffrey Horton

THREE-PHOTON MICROSCOPY AT 1,700 NM FOR *IN VIVO* IMAGING

Nicholas Geoffrey Horton, Ph. D.

Cornell University 2015

Multiphoton fluorescence microscopy (MPM) allows scientists to noninvasively observe structures deep within tissue. Two-photon microscopy (2PM) in the 750-1000 nm excitation region has been the standard MPM technique since its first demonstration in 1990. However, the maximum imaging depth for 2PM is limited by the signal-to-background ratio (SBR).

In this dissertation, three-photon imaging at 1700 nm excitation wavelength (1700 nm 3PM) is presented. The combination of the long excitation wavelength and the higher order nonlinear excitation overcomes the SBR limitations of 2PM, enabling biological investigations to take place at greater depth within tissue.

In chapter 1, tissue imaging is discussed, paying special attention to the development of laser scanning fluorescence microscopy.

In chapter 2, non-invasive, high resolution, *in vivo* imaging of subcortical structures within an intact mouse brain using 1700 nm 3PM is presented. Vascular structures as well as red fluorescent protein (RFP)-labeled neurons within the mouse hippocampus are imaged.

In chapter 3, dispersion compensation of 1700 nm 3PM is discussed. Signal generation in 3PM is proportional to the inverse-squared of the pulse width. We show that the high normal dispersion of a silicon wafer can be conveniently used to

compensate the anomalous dispersion of a 1,700 nm excitation three-photon microscope. We achieved over a factor of two reduction in pulse width at the sample, which corresponded to over a 4x increase in the three-photon signal. This signal increase was demonstrated within the mouse brain *in vivo*.

In chapter 4, through-skull imaging using 1700 nm 3PM is demonstrated. The strong scattering properties of the skull traditionally require either its partial or total removal in order to achieve a sufficient penetration depth. Skull modifications have been shown to alter brain properties, which can subsequently affect imaging experiments. We demonstrate *in vivo* vascular imaging 720 μm below the skull-brain interface through an unthinned, intact mouse skull and RFP-labeled neuron imaging 350 μm below the skull-brain interface. Our results show that long-wavelength 3PM has the potential to perform high spatial resolution *in vivo* imaging deep in the mouse brain without the removal of the skull.

BIOGRAPHICAL SKETCH

Nicholas Geoffrey Horton was born and raised in Minneapolis, Minnesota. Nick is the son of Jeffrey and Patricia Horton and the older brother of Alexander Kyle Horton and Maxwell Christian Horton. Nick's family moved to Orlando, Florida in 2001, where Nick attended Lake Brantley High School in Altamonte Springs and Rollins College in Winter Park. Nick's parents moved to Seattle, Washington in 2008, where his brothers currently reside, and then to Berkeley Heights, New Jersey in 2010.

Nick's interest in physics began with his first high school course in 2003. He majored in Physics at Rollins College, where he studied the physics of electric guitar pickups and the vibrations of hollow subterranean objects under the guidance of Dr. Thomas Moore. Nick also performed research with Dr. Lewis Duncan, who introduced him to plasma physics research at the HAARP facility in Gakona, Alaska as well as academic conferences.

Nick entered Cornell University in August 2009 with the desire to study biomedical optics. As a Presidential Life Sciences Fellow, he performed research rotations in the laboratories of Professor Chris Xu, Professor Warren Zipfel, and Professor Joseph Fetcho. Nick ultimately joined Professor Chris Xu's biomedical imaging group, where he worked to develop next-generation multiphoton microscopes for improved imaging depths. Nick also spent a summer in Professor Chen-Yuan Dong's biomedical imaging laboratory at National Taiwan University in Taipei, Taiwan as an East Asia and Pacific Life Science Institute (EAPSI) fellow, where he performed functional liver imaging using two-photon microscopy.

For Mom, Dad, Alex, and Max

ACKNOWLEDGMENTS

There are many people that I want to thank for helping me achieve this goal. I want to foremost thank Professor Chris Xu, who has given me invaluable guidance over the years. He taught me to approach problems in a logically sound way, and his financial support for research and conferences has been invaluable to the development of my professional career. I also sincerely thank Professors Chris Schaffer and Ronald Harris-Warrick for their support and advice as members of my special committee.

I want to thank members of the Xu group who helped and supported me over the years. I especially want to thank Demirhan Kobat and Ke Wang for introducing me to the research, and Kriti Charan, Dimitre Ouzounov, David Huland, Ji Cheng, Dylan Heberle, David Sinefeld, Tianyu Wang, and Tomas Rojo for making the lab experience enjoyable.

I want to thank my collaborators at Cornell University, especially Professors Chris Schaffer and Nozomi Nishimura and their students Jason Jones, Danielle Feng, JC Cruz, Catharine G. Clark, Elizabeth Wayne, Poornima Gadamsetty, and Mitch Pender for their collaboration and advice over the years. These collaborations made my time at Cornell especially enjoyable.

I would like to thank the numerous people throughout my life that brought me to a Ph.D. in Applied Physics. I want to thank Jim Helmick and Angela Cortes, my high school physics teachers, for introducing me to the wonderful field of physics, as well as Phyllis Sprinkle, my calculus teacher. I also want to thank Professors Thomas Moore, Lewis Duncan, Donald Griffin, and Elton Graugnard for advancing my knowledge and love for Physics while at Rollins College. I especially want to thank

Dr. Thomas Moore for introducing me to the field of Optics and Dr. Lewis Duncan for introducing me to academic conferences.

I would like to thank the professors who have hosted me in laboratory rotations during my graduate school years, including Professors Warren Zipfel and Joseph Fetcho at Cornell, and professor Chen-Yuan Dong at National Taiwan University.

I want to thank Susi Varvayanis for her mentorship in the Cornell Presidential Life Science Fellowship program, and the National Science Foundation for helping make my research possible through their EAPSI foreign studies program and their GRFP graduate fellowship program.

Finally, I would like to thank my mom, dad, and brothers for providing endless support over the years.

TABLE OF CONTENTS

BIOGRAPHICAL SKETCH.....	iii
ACKNOWLEDGMENTS	v
LIST OF FIGURES	ix
LIST OF TABLES	xi
LIST OF ABBREVIATIONS	xii
1. Introduction	14
1.1 Tissue imaging.....	14
1.2 Tissue selection	14
1.3 Animal selection.....	15
1.4 <i>Ex vivo</i> imaging	15
1.5 <i>In vivo</i> imaging.....	16
1.6 Advancements in <i>in vivo</i> fluorescence imaging	18
1.7 Remarks.....	21
2. <i>In vivo</i> three-photon microscopy of subcortical structures within an intact mouse brain	26
2.1 Abstract.....	26
2.2 Introduction	27
2.3 Experiment	30
2.4 Conclusion.....	36
2.5 Methods: fibre-based excitation source.....	37
2.6 Methods: imaging setup	38
2.7 Methods: animal procedures.....	40
2.8 Methods: perfusion and slicing	40
2.9 Supplementary data: comparing SBRs in 2PM and 3PM	41
2.10 Acknowledgments	45
3. Dispersion compensation in three-photon fluorescence microscopy at 1,700 nm	50
3.1 Abstract.....	50
3.2 Introduction	50
3.3 Discussion.....	57
3.4 Acknowledgments	59

4.	Imaging the mouse brain through an unthinned, intact skull using three-photon microscopy at 1,700 nm excitation	63
4.1	Abstract.....	63
4.2	Introduction	63
4.3	Results	66
4.4	Discussion.....	74
4.5	Methods: imaging setup	75
4.6	Methods: mouse preparation	76
4.7	Methods: imaging.....	77
4.8	Methods: image processing	78
4.9	Methods: skull thickness measurement	79
5.	Future experiments	86
5.1	Introduction	86
5.2	Thermal heating considerations.....	86
5.3	New applications for mouse imaging	87
5.4	Deep-tissue THG imaging.....	89
5.5	<i>In vivo</i> human tissue imaging	89
5.6	Conclusion.....	90

LIST OF FIGURES

1.1	Different imaging penetration depths and resolution limits	18
1.2	Maximum fluorescence imaging depths within the mouse brain for different LSM technologies	21
2.1	Wavelength-dependent attenuation length in brain tissue and measured laser characteristics	29
2.2	<i>In vivo</i> 3PM images of Texas-red-dextran labeled mouse brain vasculature	32
2.3	<i>In vivo</i> 3PM images of RFP-labeled neurons in mouse brain	35
2.4	Fluorescence signal attenuation curves of <i>in vivo</i> experiments	36
2.5	Resolution characterization of the 3PM	37
2.6	Comparing SBRs in 2PM and 3PM	43
2.7	3PM experimental Setup	44
2.8	Epifluorescence images of the B6.Cg-Tg(Thy1-Brainbow1.0)HLich/J mouse brain	45
3.1	Material GVD vs. wavelength near 1,700 nm for common optical materials	53
3.2	Experimental Setup	53
3.3	Spectrum of pulse and second-order interferometric autocorrelations after various optical elements	55
3.4	<i>In vivo</i> three-photon microscopy of Texas Red-labeled blood vessel within an intact mouse brain.	56
3.5	TOD of common optical materials	58
4.1	Through-skull imaging locations of a mouse with Texas-Red labeled vasculature	67
4.2	Through-skull imaging of the vasculature of mouse brain. The skull-brain interface is observed by boundaries in the fluorescence and THG channels	68
4.3	Signal attenuation before and after craniotomy.	70

4.4	Axial Resolution comparisons of vascular imaging, and signal profile of a blood vessel in the deepest recorded vasculature fluorescence frame	72
4.5	Three-dimensional rendering of RFP-labeled neurons in a mouse brain.	73
4.6	Frames from 8-week old RFP mouse.	74
4.7	Microscope setup, and the laser profile and second-order interferometric autocorrelation, assuming a sech^2 pulse.	80
4.8	Signal decay curve of the RFP mouse.	80
4.9	Resolution tests of an RFP-labeled feature.	81

LIST OF TABLES

3.1	Calculated GVD and TOD of various materials at 1,700 nm.	58
-----	--	----

LIST OF ABBREVIATIONS

2PM	Two-Photon Microscopy
3PE	Three-Photon Excitation
3PM	Three-Photon Microscopy
AO	Adaptive Optics
CA1	Cornu Ammonis 1 (region of the hippocampus)
CAL	Characteristic Attenuation Length
CT	Computer Tomography
EC	External Capsule
FOV	Field-of-view
FWHM	Full Width at Half Maximum
GDD	Group Delay Dispersion
GVD	Group Velocity Dispersion
LSM	Laser Scanning Microscopy
MHz	Megahertz
MRI	Magnetic Resonance Imaging
NA	Numerical Aperture
OCT	Optical Coherence Tomography
PC	Photonic Crystal
PC	Post-Crainotomy
PET	Positron Emission Tomography
PM	Polarization-maintained

PMT	Photomultiplier Tube
QE	Quantum Efficiency
RFP	Red Fluorescent Protein
SBR	Signal-to-Background Ratio
SNR	Signal-to-Noise Ratio
SP	<i>Stratum Pyramidale</i> (region of the hippocampus)
TOD	Third-Order Dispersion
TS	Through-skull (i.e., no skull polishing, thinning or removal)

CHAPTER 1

INTRODUCTION

1.1 Tissue imaging

Biological imaging is critical for understanding tissue structure and function and has especially important applications for studying disease progression. This dissertation focuses on development of three-photon microscopy (3PM) for *in vivo* imaging of the mouse brain using 1,700 nm excitation light, which currently holds the record for high-contrast, high-resolution microscopy deep within *in vivo* biological tissue. This chapter briefly discusses the significance of brain research, the relevance of mouse models, and how 3PM compares with other imaging techniques.

1.2 Tissue selection

The brain is an extremely complex organ that is currently poorly understood. Improvements in imaging technologies should help allow scientists to unravel its mysteries. In addition to the purely scientific desire to better understand the brain, significant progress has also been made to study diseases such as Alzheimer's [1], Parkinson's [2], and Multiple Sclerosis [3], and imaging techniques are critical in the search for cures [4,5]. Further improvements of brain imaging are especially important because these will allow exploring deeper regions of the brain with even higher resolution, which could lead to more rapid medical breakthroughs.

1.3 *Animal selection*

Selecting a proper animal for neural imaging is important and should reflect experiment goals. Primitive animals such as zebrafish and *C. Elegans* are beneficial for neural network imaging because their circuits are relatively simple and their bodies are relatively transparent, which allows deep imaging even with high-resolution techniques [6–8]. However, these animals lack the complex brain anatomy of humans and therefore cannot be used for some important brain function studies and as disease models. On the other end of the animal spectrum, practical and ethical issues prevent primates from widespread use in standard laboratories. Somewhere between these two extremes are mice, which are an ideal choice because they are small (~25 g), easy to breed, and their brains are structurally similar to humans [9]. Because the benefits of mouse imaging are well-known, there is already a large catalog of inbred mouse strains available from vendors such as The Jackson Laboratory and Charles River Laboratories. For example, dozens of mouse strains possess fluorescent proteins pre-loaded into the genetics, and dozens of other mouse strains can mimic disease progression such as Alzheimer's and Parkinson's. In order to best utilize these pre-existing mouse strains, new imaging technologies that can utilize these existing strains are especially useful.

1.4 *Ex vivo imaging*

The first biological imaging studies, published in Robert Hooke's *Micrographia* in 1665, used *ex vivo* white light microscopy. Despite its status as the oldest imaging technique, advancements in *ex vivo* imaging technologies are still

making headlines, especially regarding brain imaging. New optical clearing technologies allow selective imaging of neurons throughout the entire brain with submicron resolution [10–12], and an enormous undertaking to image the brain with 4-nm resolution using electron microscopy is also underway [13].

Advantages of *ex vivo* imaging are that the tissues can be sliced to image any region within the sample, and proper preservation techniques can allow long-term repeat imaging. *Ex vivo* tissue imaging is especially important for the field of pathology, where it is the current standard for cancer detection. While *ex vivo* imaging is helpful for understanding tissue structure and pathology, it is incapable of observing short-term tissue dynamics as well as long-term tissue development and disease progression.

1.5 In vivo imaging

In vivo imaging is valuable for studying tissue dynamics. However, *in vivo* imaging introduces challenges that are not present in *ex vivo* imaging: tissue configurations within animals prevent easy access of certain regions (e.g., the brain's dorsal side is its only accessible region), and each technology offers a tradeoff between resolution and imaging depth (Fig. 1). Furthermore, a specific imaging technique has greater utility if it can excite a diverse catalog of contrast agents. Magnetic resonance imaging (MRI), photoacoustic tomography, positron emission tomography (PET), computer tomography (CT), ultrasound, photoacoustic, optical coherence tomography (OCT), and fluorescence microscopy are common techniques for *in vivo* imaging with various advantages and disadvantages. MRI, PET, ultrasound,

and CT in general are capable of imaging through the entire mouse brain and also allow various contrast agents for highlighting specific structures; however, these techniques also suffer from relatively poor resolution ($>50\mu\text{m}$). While this resolution is generally sufficient for studying functional blood flow or tumor development, it is insufficient for observing individual cells and interactions between them. Higher-resolution techniques such as photoacoustic and OCT imaging permit relatively deep imaging with near-cellular resolution, but their contrast agent selections are limited (e.g. gold nanoparticles) [14,15].

Fluorescence imaging is capable of producing sub- μm lateral and subcellular axial resolution, and is commonly used to image capillaries ($\sim 3\ \mu\text{m}$ diameter), cells ($\sim 10\ \mu\text{m}$ in diameter), and neural processes (e.g., axons, $<1\ \mu\text{m}$ diameter) [16], and can utilize a large variety of fluorescent probes which can even be multiplexed for simultaneous imaging of different structures. Laser scanning fluorescence microscopy (LSM) [17] is a specific subset of fluorescence imaging that is especially useful for three-dimensional optical sectioning of tissue. However, this technology in its most basic form (i.e., confocal LSM) only allows a relatively small penetration depth into tissue [18]. Multiphoton fluorescence microscopy, which utilizes the same fluorophores for confocal imaging yet allows significantly deeper penetration depth (Fig. 1.1), is arguably the most significant advancement for high spatial resolution *in vivo* imaging in the last 25 years and is discussed further in the next section.

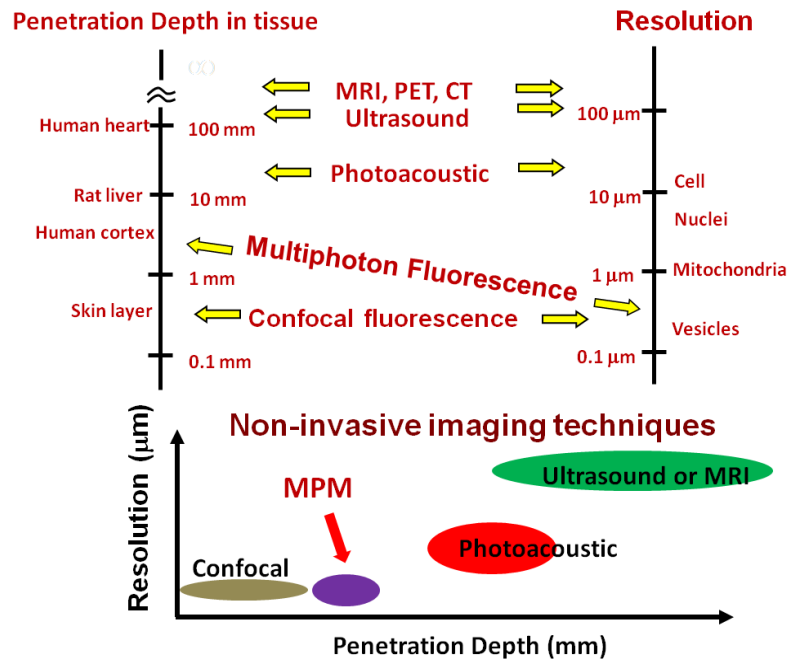


Fig. 1.1 Different imaging penetration depths and resolution limits. Multiphoton microscopy is the best technique for high-resolution imaging deep within tissue.

1.6 Advancements in in vivo fluorescence imaging

Confocal laser scanning microscopy, introduced in 1969 [19,20], is the oldest laser scanning fluorescence microscopy technique and is still commonly used today [21,22]. This technique utilizes a pinhole placed at the conjugate image plane. Fluorescent dyes within the sample are excited by the laser, and any unscattered light that is generated at the focus of the microscope objective ultimately passes through the pinhole and onto the detector; any unscattered light that is generated away from the focal plane is rejected by the pinhole. Because confocal fluorescence is a one-photon absorption process, the pinhole is necessary to remove any light that isn't generated at the focus. Deep imaging is possible as long as the tissue isn't scattering (e.g., within

the vitreous of the eye [23]), because even minimal scattering will wash out the signal. For example, *in vivo* brain imaging is only possible down to $\sim 150 \mu\text{m}$ in the brain using this technique [18].

Two-photon fluorescence microscopy (2PM) was first demonstrated by Denk, Strickler, and Webb in 1990 and revolutionized the field of deep-tissue *in vivo* fluorescence imaging [24]. Other sources discuss multiphoton microscopy theory in great detail [25]; this introduction is meant to merely highlight its advantages over other imaging techniques. The nonlinear nature of two-photon absorption results in absorption that occurs almost exclusively from ballistic photons in the perifocal region, which eliminates the need for a pinhole and allows the use of large-area detectors. Furthermore, the titanium:sapphire oscillator, which offers a tunable range of excitation wavelengths between 650 and 1100 nm and a repetition rate around 100 MHz, is ideal for exciting dyes that were previously used for one-photon imaging. Soon after the first demonstration of 2PM, biologists were able to perform *in vivo* brain imaging up to $600 \mu\text{m}$ within the $\sim 850 \mu\text{m}$ thick mouse cortex. However, the practical deep-imaging limit of two-photon imaging is where the signal-to-background ratio (SBR) equals 1, which is the depth that fluorescence generated within surface layers of the tissue generate the same amount of signal as the ballistic photons at the focus. Modifications to this standard setup, such as the use of a regenerative amplifier [26], multi-watt laser [27], and a longer excitation wavelength [28,29], made it possible to penetrate the underlying white matter and hippocampus. Although these enhanced techniques have been used to image the hippocampus, their SBR is roughly 1 at these depths. The lack of high-SBR deep imaging technologies led scientists to

insert penetrating optical elements or remove overlying tissue in order to image at the desired depths [30,31]. Although great care is taken not to damage the tissue in these experiments, the animal preparation is not ideal because any modifications of the brain could affect experiments.

Three-photon fluorescence is an improvement over two-photon imaging because the SBR is orders of magnitude higher within the mouse brain [16]. This technique required new laser sources that produced long-wavelength (~ 1700 nm), low repetition-rate (~ 1 MHz), high pulse energy (~ 100 nJ), short temporal width (~ 60 fs) pulses in order to generate adequate three-photon signals. Because of the high SBR for three-photon microscopy (see Chapter 2), future improvements with the laser source will permit even deeper 3P imaging. The following chapters focus on three-photon imaging using 1700 nm excitation light and show the significant improvements in imaging depth that can be achieved with this technique. Fig. 1.2 provides a visual summary of maximum imaging depths within the mouse brain for different fluorescence LSM technologies.

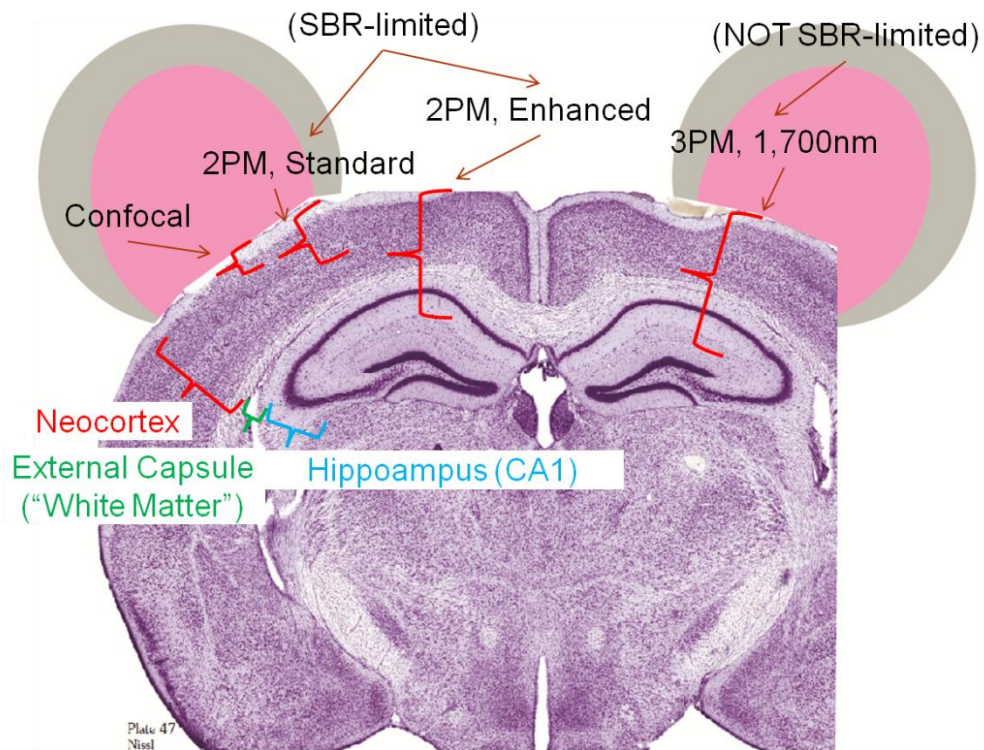


Fig. 1.2: Maximum fluorescence imaging depths within the mouse brain for different LSM technologies. “2PM, Standard” is 800 nm excitation wavelength, 80 MHz repetition rate. “2PM, Enhanced” refers to high pulse energies, high average powers, and longer excitation wavelengths. Both of these techniques are SBR-limited at their maximum depths. 3PM is not SBR-limited, and more energetic laser sources will permit deeper imaging.

1.7 Remarks

There is no single best method for *in vivo* tissue imaging. However, within each imaging technology, certain systems are more effective than others. Fluorescence imaging allows the highest possible resolution and the greatest ability of selective labeling of *in vivo* tissue structures of the aforementioned imaging technologies, and three-photon imaging at 1,700 nm excitation offers the deepest imaging using this technique.

REFERENCES

1. Y. Huang and L. Mucke, "Alzheimer mechanisms and therapeutic strategies," *Cell* **148**, 1204-1222 (2012).
2. B.S. Connolly and A. Lang, "Pharmacological treatment of Parkinson Disease: a review," *JAMA-J. Am. Med. Assoc.* **311**, 1670-1683 (2014).
3. M. Inglese, "Multiple Sclerosis : new insights and trends," *AJNR-Am. J. Neuroradiol.* (2006).
4. J. J. Iliff, M. Wang, Y. Liao, B.A. Plogg, W. Peng, G.A. Gundersen, H. Benveniste, G. E. Vates, R. Deane, S.A. Goldman, E.A. Nagelhus, and M. Nedergaard, "A paravascular pathway facilitates CSF flow through the brain parenchyma and the clearance of interstitial solutes, including amyloid β ," *Sci. Translation. Med.* **4**, 147ra111 (2012).
5. M.J. Farrar, F.W. Wise, J.R. Fetcho, and C.B. Schaffer, "In vivo imaging of myelin in the vertebrate central nervous system using third harmonic generation microscopy," *Biophys. J.* **100**, 1362-1371 (2011).
6. A. Muto, M. Ohkura, T. Kotani, S.-I Higashijima, J. Nakai, and K. Kawakami, "Genetic visualization with an improved GCaMP calcium indicator reveals spatiotemporal activation of the spinal motor neurons in zebrafish.," *PNAS* **108**, 5425-30 (2011).
7. L. C. Leung, G. X. Wang, and P. Mourrain, "Imaging zebrafish neural circuitry from whole brain to synapse," *Front. in Neur. Circ.* **7**, 76 (2013).

8. J. Larsch, D. Ventimiglia, C. I. Bargmann, and D. R. Albrecht, "High-throughput imaging of neuronal activity in *Caenorhabditis elegans*," *PNAS* **110**, E4266-E4273 (2013).
9. P. P. G. Allen, "Observatories of the mind," *Nature* **483**, 397-398 (2012).
10. H.-U. Dodt, U. Leischner, A. Schierloh, N. Jahrling, C. P. Mauch, K. Deininger, J. M. Deussing, M. Eder, and W. Zieglgansberger, and K. Becker, "Ultramicroscopy : three-dimensional visualization of neuronal networks in the whole mouse brain," *Nat. Method.* **4**, 331-336 (2007).
11. H. Hama, H. Kurokawa, H. Kawano, R. Ando, T. Shimogori, H. Noda, K. Fukami, A. Sakaue-sawano, and A. Miyawaki, "Scale : a chemical approach for fluorescence imaging and reconstruction of transparent mouse brain," *Nature Neuroscience* **14**, 1481-1488 (2011).
12. M.-T Ke, S. Fujimoto, and T. Imai, "SeeDB: a simple and morphology-preserving optical clearing agent for neuronal circuit reconstruction," *Nat. Neurosci.* **16**, 1154-1161 (2013).
13. V. Marx, "Brain mapping in high resolution," *Nature* **503**, 147-152 (2013).
14. G. Liu and Z. Chen, "Optical Coherence Tomography for Brain Imaging," *Optical methods and instrumentation in brain imaging and therapy*, Chapter 7 157-172 (2013).
15. O. Assayag, K. Grieve, B. Devaux, F. Harms, J. Pallud, F. Chretien, C. Boccarda, and P. Varlet, "Imaging of non-tumorous and tumorous human brain tissues with full-field optical coherence tomography," *Neuroim.: clin.* **2**, 549-557 (2013).

16. N. G. Horton, K. Wang, D. Kobat, C. G. Clark, F. W. Wise, C. B. Schaffer, and C. Xu, "In vivo three-photon microscopy of subcortical structures within an intact mouse brain," *Nat. Photon.* **7**, 205-209 (2013).
17. J. S. Ploem, "Laser scanning fluorescence microscopy," *Appl. Opt.* **26**, 3226-3231 (1987).
18. Y. Takahara, N. Matsuki, and Y. Ikegaya, "Nipkow confocal imaging from deep brain tissues," *J. Integr. Neurosci.* **10**, (2011).
19. P. Davidovits and M. D. Egger, "Scanning Laser Microscope," *Nature* **223**, 831 (1969).
20. P. Davidovits and M. D. Egger, "Scanning Laser Microscope for Biological Investigations," *Appl. Opt.* **10**, 1615-1619 (1971).
21. P.-Y. Lam, R. S. Fischer, W. D. Shin, C. M. Waterman, and A. Huttenlocher, "Spinning Disk Confocal Imaging of Neutrophil Migration in Zebrafish," *Neutrophil methods and protocols, methods in molecular biology, Chapter 14* **1124**, 219-233 (2014).
22. T. Wilson, "Resolution and optical sectioning in the confocal microscope," *J. Microsc.* **244**, 113-121 (2011).
23. D. V. Patel and C. N. McGhee, "Quantitative analysis of in vivo confocal microscopy images : a review," *Surv. Ophthalmol.* **58**, 466-475 (2013).
24. W. Denk, J. H. Strickler, and W. W. Webb, "Two-photon laser scanning fluorescence microscopy," *Science* **248**, 73-76 (1990).

25. C. Xu and W. W. Webb, "Multiphoton Excitation of Molecular Fluorophores and Nonlinear Laser Microscopy," in *Topics in Fluorescence Spectroscopy*, J. R. Lakowicz, ed. (Plenum, 1997), Vol. 5, pp. 471-540.
26. P. Theer, M. T. Hasan, and W. Denk, "Two-photon imaging to a depth of 1000 microm in living brains by use of a Ti:Al₂O₃ regenerative amplifier," *Opt. Lett.* **28**, 1022-1024 (2003).
27. R. Kawakami, K. Sawada, Y. Kusama, Y.-C. Fang, S. Kanazawa, Y. Kozawa, S. Sato, H. Yokoyama, and T. Nemoto, "In vivo two-photon imaging of mouse hippocampal neurons in dentate gyrus using a light source based on a high-peak power gain-switched laser diode," *Biomed. Opt. Exp.* **6**, 891-901 (2015).
28. D. Kobat, M. E. Durst, N. Nishimura, A. W. Wong, C. B. Schaffer, and C. Xu, "Deep tissue multiphoton microscopy using longer wavelength excitation," *Opt. Exp.* **17**, 13354-13364 (2009).
29. D. Kobat, N. G. Horton, and C. Xu, "In vivo two-photon microscopy to 1.6-mm depth in mouse cortex.," *J. Biomed. Opt.* **16**, 106014 (2011).
30. M. J. Levene, D. A. Dombeck, K. A. Kasischke, R. P. Molloy, and W. W. Webb, "In vivo multiphoton microscopy of deep brain tissue.," *J. Neurophysiol.* **91**, 1908-1912 (2004).
31. D. A. Dombeck, C. D. Harvey, L. Tian, L. L. Looger, and D. W. Tank, "Functional imaging of hippocampal place cells at cellular resolution during virtual navigation," *Nat. Neurosci.* **13**, 1433-1440 (2010).

CHAPTER 2

IN VIVO THREE-PHOTON MICROSCOPY OF SUBCORTICAL STRUCTURES WITHIN AN INTACT MOUSE BRAIN¹

2.1 *Abstract*

Two-photon fluorescence microscopy (2PM) [1] enables scientists in various fields including neuroscience [2,3], embryology [4], and oncology [5] to visualize *in vivo* and *ex vivo* tissue morphology and physiology at a cellular level deep within scattering tissue. However, tissue scattering limits the maximum imaging depth of 2PM within the mouse brain to the cortical layer, and imaging subcortical structures currently requires the removal of overlying brain tissue [3] or the insertion of optical probes [6,7]. Here we demonstrate non-invasive, high resolution, *in vivo* imaging of subcortical structures within an intact mouse brain using three-photon fluorescence microscopy (3PM) at a spectral excitation window of 1,700 nm. Vascular structures as well as red fluorescent protein (RFP)-labeled neurons within the mouse hippocampus are imaged. The combination of the long excitation wavelength and the higher order nonlinear excitation overcomes the limitations of 2PM, enabling biological investigations to take place at greater depth within tissue.

¹ The contents of this chapter have been reproduced from Nature Photonics 7(5), 205-209 (2013).

2.2 Introduction

Optical imaging plays a major role in both basic biological research and clinical diagnostics, providing a non-invasive or minimally-invasive microscopic imaging capability to investigate biological tissue. Optical image acquisition through significant depths of biological tissue, however, presents a major scientific challenge since tissue is extremely heterogeneous and the strong scattering of the various tissue components has historically restricted high-resolution optical imaging to thin sections or to superficial layers. The development of 2PM has significantly extended the penetration depth of high-resolution optical imaging, particularly for *in vivo* applications [8-12]. In the last 20 years, 2PM has enabled, in many fields for the first time, direct visualization of the normal behaviour of cells in their natural environment as well as their responses to systematic manipulations [3,13]. Two-photon excitation of fluorescent molecules in tissue depends on the ability of sufficient excitation light to reach the focus of the objective unscattered (i.e., ballistic excitation photons). The fundamental limitation on imaging depth for high-resolution 2PM is the signal-to-background ratio (SBR) of the excitation in scattering biological tissue [10,12] (derivation of SBR for 2PM in section 2.9), which for 2PM is typically between 5 and 6 effective attenuation lengths (l_e) below the tissue surface. For example, for 2PM in the mouse neocortex at 775-nm excitation ($l_e \sim 130 \mu\text{m}$), this depth limit is $\sim 700 \mu\text{m}$. An effective strategy for increasing the maximum imaging depth is using longer excitation wavelengths to reduce the attenuation of excitation light by tissue [11,12,14,15]. The optimum spectral window for excitation is determined by the trade-off between tissue scattering and absorption (typically dominated by water

absorption in the near-infrared spectral region). Figure 2.1a shows the water absorption length (l_a) [16] and the calculated scattering length (l_s) of mouse brain tissue [10,12]. The combined effect of absorption and scattering is represented by l_e [i.e., $l_e=(1/l_a+1/l_s)^{-1}$]. Figure 2.1a clearly indicates that the optimum wavelength window in terms of tissue penetration is near 1,700 nm when both tissue scattering and absorption are considered.

A longer excitation wavelength alone cannot overcome the depth limit imposed by the SBR of 2PM. 3PM was first demonstrated in the 1990s [17-19], mainly to extend the spectral range of the excitation source (e.g., access the transition band from 230 to 300 nm using a mode-locked Titanium:Sapphire laser). A significant advantage of 3PM that has been largely overlooked is that three-photon excitation (3PE) provides significant improvement in the overall excitation localization [17]. The fluorescence of 3PE falls off as $\sim 1/z^4$ (where z is the distance away from the focal plane), while the fluorescence of two-photon excitation (2PE) falls off as $\sim 1/z^2$. Therefore, 3PE dramatically reduces the out-of-focus background in regions far away from the focal plane, improving the SBR by orders of magnitude when compared to 2PE (see Fig. 2.6). In addition, 3PE allows a wide variety of existing fluorescent dyes, fluorescent proteins, and calcium indicators to be excited at the 1,700-nm spectral window (equivalent to a one-photon excitation of ~ 560 nm), eliminating the practical difficulty caused by the lack of fluorescent indicators at the 1,700-nm spectral excitation window for 2PE as well as the lack of good potential fluorescence detectors for the near infrared wavelengths at which such dyes would likely emit.

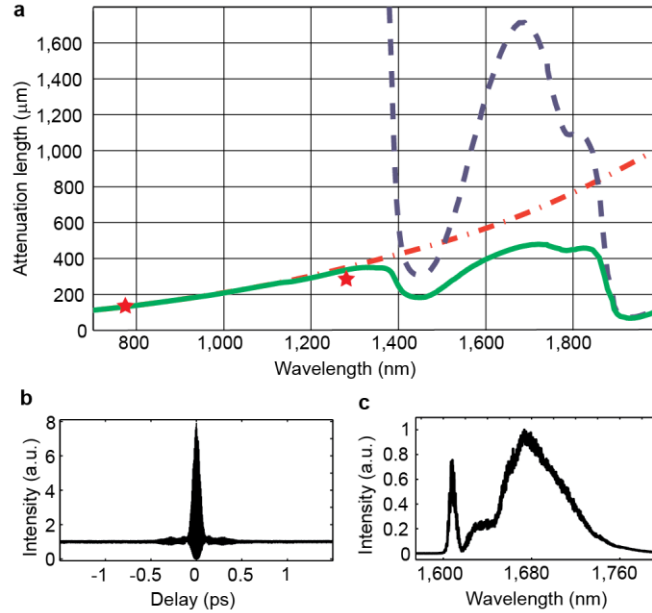


Figure 2.1: Wavelength-dependent attenuation length in brain tissue and measured laser characteristics. a, Attenuation spectrum of a tissue model based on Mie scattering and water absorption, showing the absorption length of water (blue dash line), the scattering length of mouse brain cortex (red dash-dot line), and the combined effective attenuation length (green solid line). The scattering length is calculated using Mie theory for a tissue-like phantom solution containing $1\ \mu\text{m}$ diameter polystyrene beads at a concentration of $5.4 \times 10^9/\text{ml}$, which resembles the scattering property of the cortex (i.e., grey matter). The red stars indicate the reported attenuation lengths for mouse cortex *in vivo* from previous work [11]. b, c, The measured second-order interferometric autocorrelation trace (b) and the corresponding spectrum (c) of the 1,675-nm soliton generated in the PC rod. The soliton energy, integrated from 1,617 nm, is 67 nJ.

The amount of 3PE can be significantly increased by using a low duty cycle, high pulse-energy excitation source [17], while still maintaining a low average power that does not cause tissue heating [11]. We developed a novel high pulse-energy source at 1,675 nm (Fig. 2.1c) using soliton self-frequency shift (SSFS) [20,21] in a photonic crystal (PC) rod [22] pumped by a turn-key, energetic fibre laser at 1,550 nm (see section 2.5 for details). The large mode-field area of the PC rod enables the

generation of high soliton pulse energy for 3PE. The measured output soliton energy of our source is 67 nJ at 1 MHz repetition rate, which is the highest soliton energy ever achieved through SSFS in a solid-core fibre. The measured soliton pulse width is 65 fs (Fig. 2.1b). SSFS not only shifts the wavelength to the desired 1,700 nm spectral window but also compresses the pulse width by a factor of 6, both essential for deep tissue 3PM.

2.3 Experiment

We performed *in vivo* imaging of mouse brain vasculature to demonstrate the capability of deep tissue imaging at 1,675 nm using 3PE. The vasculature was labelled by a retro-orbital injection of dextran-coupled Texas Red dye (Invitrogen). We acquired a 1,400 μm deep stack, taken with 4 μm depth increments. Figure 2.2a shows the 3D reconstruction of the data. By employing the energetic excitation source we developed at $\sim 1,700$ nm, the average power required for 3PM at the surface of the brain in our experiments is ~ 3 mW, which is comparable to conventional 2PM. For optical sections within the first 0.8 mm of imaging depth, the excitation powers were adjusted so that approximately the same signal level, and thus the same signal-to-noise ratio (SNR), could be achieved at a constant frame time of 8 seconds (512×512 pixels per frame). Our excitation source was used at full power (22 mW at the sample surface) at depths beyond 0.8 mm, while the integration time was increased 2.5 times (20 s/frame). The myelinated axons in the external capsule (EC, a.k.a. “white matter”) produce a bright third harmonic generation (THG) signal [23-25] (Figs. 2.2a,b), which delineates the boundaries of the EC. Our images show that the EC begins

approximately 840 μm below the surface of the brain. The EC is approximately 116 μm thick, and the CA1 region of the hippocampus (CA1) begins approximately 956 μm below the surface of the brain. We were able to obtain high-resolution, high-contrast images of the blood vessels up to approximately 1,300 μm deep. From this data set, it is possible to determine a characteristic attenuation length (CAL) for 1,675-nm imaging in mouse brain tissue *in vivo*. For 3PE, we define the CAL as the depth at which the average fluorescence signal of the brightest 0.1% of pixels attenuates by $1/e^3$. Figure 4a shows the detected fluorescence signal as a function of imaging depth, from which the CALs are determined to be 365 μm between 56 μm and 840 μm (i.e., the neocortex), 137 μm between 840 μm and 956 μm (i.e., the EC), and 310 μm between 956 μm and 1,148 μm (i.e., the CA1). In comparison, we had previously measured the CAL of the cortex to be 131 μm at 775 nm and 285 μm at 1,280 nm [11,12]. Furthermore, with 2PM at 1280 nm, we were unable to penetrate the EC using the same aged animals at the same sagittal and coronal imaging position as reported here [12].

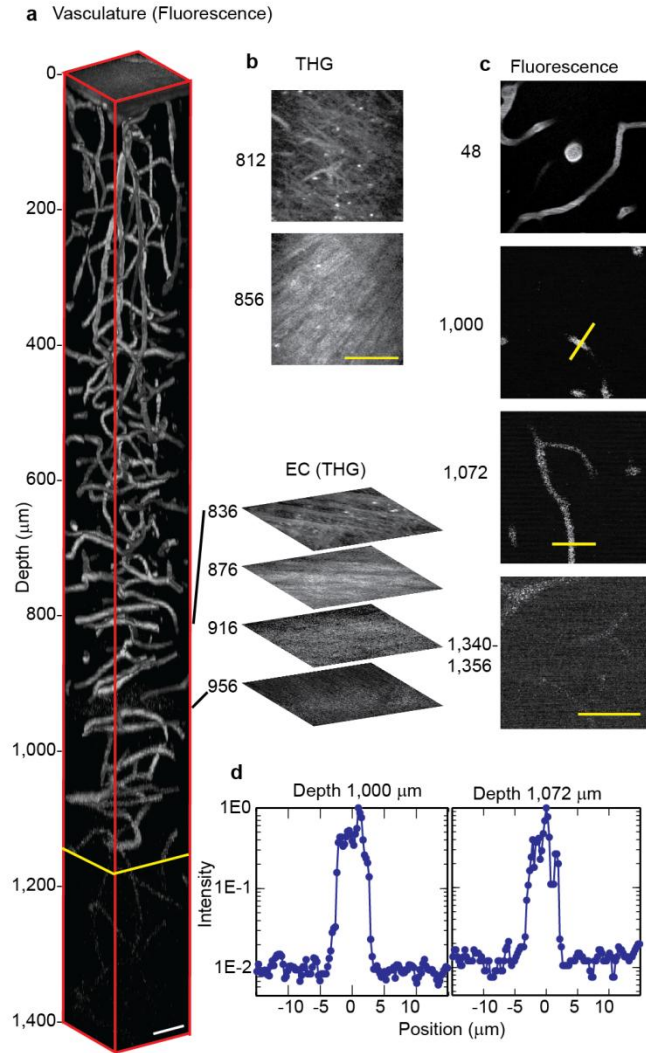


Figure 2.2: *In vivo* 3PM images of Texas-red-dextran labeled mouse brain vasculature. a, 3D reconstruction of 3PM images of the brain of an FVB/N mouse. The EC extends from approximately 840 to 956 μm below the surface of the brain. Frames deeper than 1,136 μm (yellow line) were normalized to the frame at 1,136 μm ; all other frames were individually normalized. The expanded optical sections to the right are representative THG images from the EC region of the brain. b, c, d, Normalized x-y frames of the THG (b) and fluorescence signal (c) at various depths. The bottom frame in (c) is a z projection of 20 μm . The fluorescence profiles of the lines across the vessels in (c) are displayed in semi-logarithmic plots (d), which are used for the SBR calculation. Background is calculated by averaging the intensity values between -15 and -5 μm and between 5 and 15 μm . All scale bars are 50 μm .

We also performed quantitative SBR measurements at four depths between 1,000 and 1,135 μm (i.e., within the CA1). The SBRs range from 79 to 119; two examples are shown in Figs. 2.2c,d. The measured SBRs are lower than predicted by theory (shown in Fig. 2.6) due to the limited SNR of the images (signal level vs. the electronic noise floor) at these depths. Nonetheless, these SBR values are more than one order of magnitude higher than previous 2PM results at 1,280 nm at similar depths but without the presence of the highly scattering EC [12].

We also imaged RFP-labelled neurons in a B6.Cg-Tg(Thy1-Brainbow1.0)HLich/J mouse [26] through a cranial window (see Methods). In particular, the labelled cells include pyramidal neurons in the neocortex and the *stratum pyramidale* (SP), a dense layer of pyramidal neurons within the hippocampus. We acquired a 1,220 μm stack, taken with 4 μm depth increments. Imaging conditions were similar to those used in Fig. 2.2, except that our source was used at full power (22 mW) at 0.7 mm, and starting from 0.74 mm, the integration time was increased 2 times (16 s/frame). Beyond 0.9 mm, the integration time was increased by another 1.25 times (20 s/frame). Figure 2.3a shows the 3D reconstructions of the data along with selected optical sections of the SP region. Bright fluorescence images with appearance nearly identical to THG images are obtained in the EC, indicating expression of RFP in the axons in EC (Fig. 2.3c,d). Labelled neurons in the SP can be seen 1,060-1,120 μm below the surface of the brain (Fig. 2.3a,c). Visualization of this layer is clear evidence of direct imaging of the mouse hippocampus through an intact brain (see Figs. 2.3b and 2.8) [27]. Figure 2.4b shows the detected fluorescence signal as a function of imaging depth. From the slope of the line, we measured the CAL to be

401 μm between 36 μm and 840 μm (i.e., the neocortex) and 229 μm between 840 μm and 976 μm (i.e., the EC). The relative increase in signal at 1.1 mm is due to the cells in the SP. The fluorescence value was uneven within the hippocampus due to the layered distribution of the pyramidal neurons, which made a CAL calculation difficult in this region.

We measured the lateral brightness distribution of small features within the RFP-labelled mouse brain (Fig. 2.5a,b), which provides the upper bound of the lateral resolution. For example, at 644 μm and 844 μm depths of the mouse brain, the full widths at half maximum (FWHM) of lateral brightness distributions are $\sim 0.9 \mu\text{m}$. The axial FWHM are measured to be between 5.1 and 5.5 μm (average 5.3 μm) for 5 capillary blood vessels at depths between 817 and 948 μm below the surface of the brain (two examples are shown in Figs. 2.5c,d). Taking into account that the minimum diameter of mouse capillary is $\sim 3 \mu\text{m}$ [28], these values indicated that the axial resolution (FWHM) of our system is $\sim 4.4 \mu\text{m}$ at these depths.

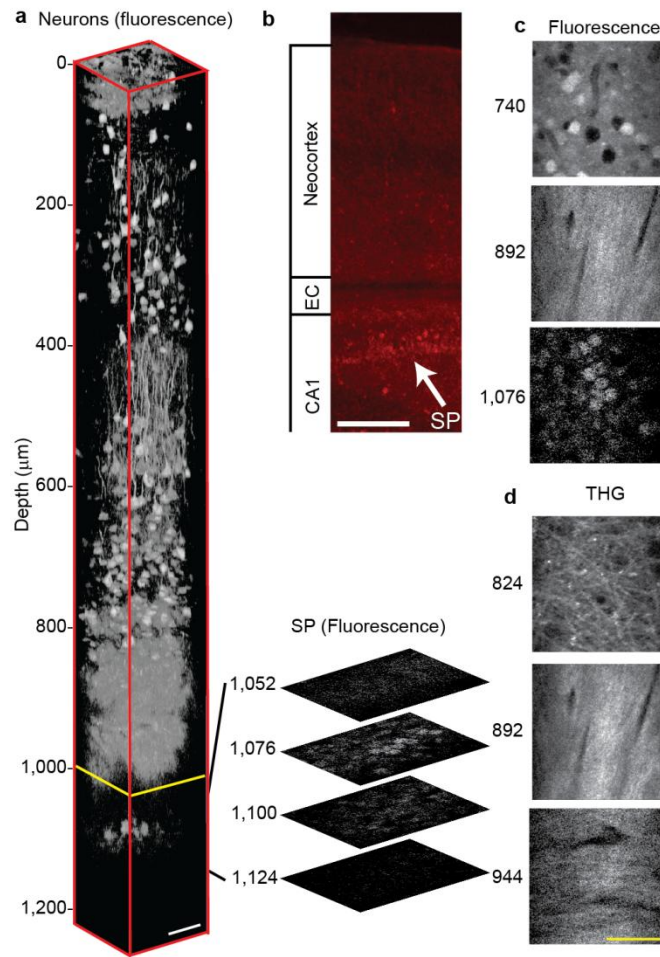


Figure 2.3: *In vivo* 3PM images of RFP-labeled neurons in mouse brain. a, 3D reconstruction of 3PM images in the brain of a B6.Cg-Tg(Thy1-Brainbow1.0)HLich/J mouse, which contains RFP-labelled pyramidal neurons. Frames deeper than 992 μm (yellow line) were normalized to the frame at 1,076 μm (i.e., the SP); all other frames were individually normalized. The expanded optical sections to the right are representative fluorescence images of the SP. The EC extends from approximately 840 to 976 μm below the surface of the brain, and the SP extends from approximately 1,060 to 1,120 μm below the surface. The scale bar is 50 μm . b, Epifluorescence image of the coronal section of the mouse brain at approximately the same location to that shown in (a). The white arrow indicates the SP. The scale bar is 250 μm . c, d, Normalized x-y frames of the fluorescence (c) and THG (d) signal at various depths. The scale bar is 50 μm .

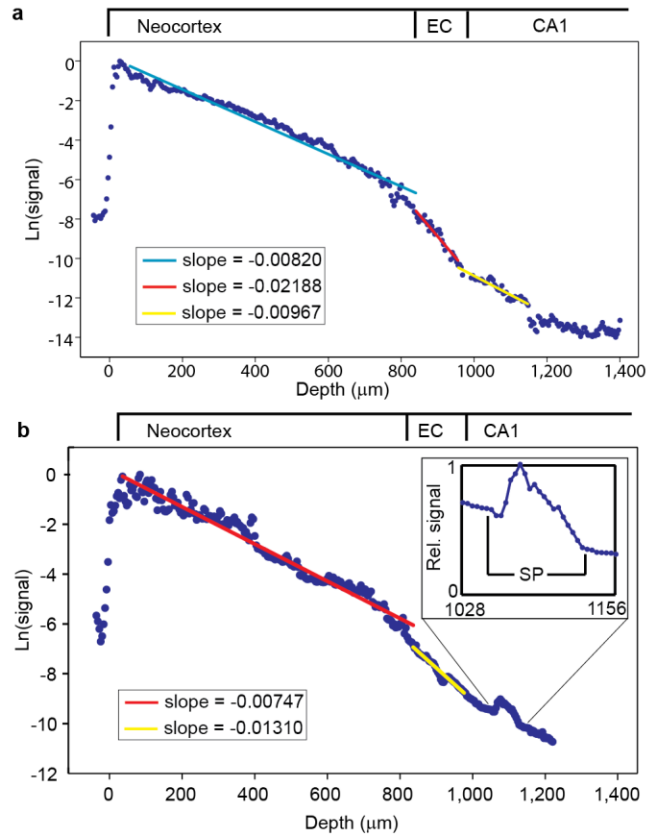


Figure 2.4: Fluorescence signal attenuation curves of *in vivo* experiments. a, b, Semi-logarithmic plots of the fluorescence signal of the images in Fig. 2.2a (a) and Fig. 2.3a (b), normalized to the cubic of the laser power versus depth.

2.4 Conclusion

3PM at the new spectral window of 1,700 nm is potentially a powerful new tool for *in vivo*, high-resolution, deep tissue imaging. By further improving the excitation source and microscope optics at 1,700 nm, we estimate that at least one order of magnitude improvement in frame rate can be achieved. In addition, by increasing the energy of the pump pulse and optimizing the PC rod, a wavelength tuneable source that covers the entire “low attenuation” spectral window from 1,650 to

1,850 nm can be obtained, which will further increase the number of accessible fluorophores and fluorescent proteins for 3PE in the 1,700-nm spectral window.

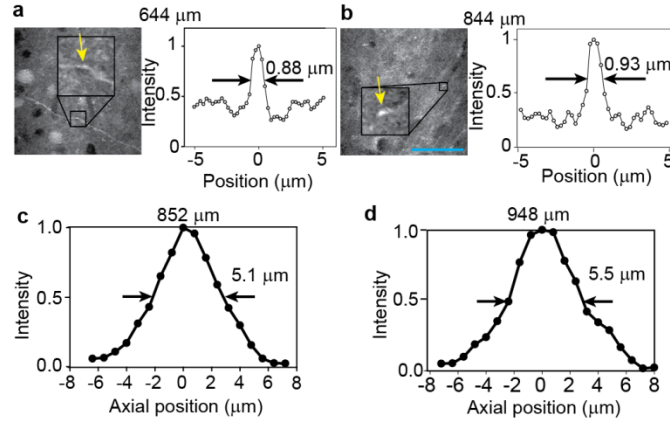


Figure 2.5: Resolution characterization of the 3PM. Intensity line profiles are used to characterize the lateral resolution. a, b, Sample x-y frames at 644 μm (a) and 844 μm depth (b) of the B6.Cg-Tg(Thy1-Brainbow1.0)HLich/J mouse, where a line profile on the right is taken across a labelled neural process (indicated by yellow arrows). The scale bar is 50 μm . c, d, Axial measurements of FVB/n mouse Texas-red stained capillary vessels at 852 μm (c) and 948 μm (d) depth.

2.5 Methods: fibre-based excitation source

The pump source for SSFS is a compact, turn-key, fibre-based femtosecond laser (FLCPA-01C, Calmar), delivering 360 fs and linearly-polarized pulses with a 1 MHz repetition rate at 1,550 nm. SSFS is performed in a commercially available, 36 cm long, polarization maintained (PM) PC rod (DC-200-70-PM-Yb-ROD, NKT Photonics) with an effective mode area (A_{eff}) of 2,300 μm^2 at 1,550 nm. After collimation, a 1,600 nm long pass filter (LPF, 1600ALP, Omega Optical) is used to filter out the residual pump. The soliton shifts to 1,675 nm at an input pulse energy of

500 nJ. The pulse width of the soliton is measured by performing second order autocorrelation. The measured soliton pulse width, assuming a sech^2 intensity profile, is 65 femtoseconds (fs) (Fig. 2.1b). Due to the dispersion of microscope optics, the pulse width broadened to 79 fs after the objective. Pulse broadening due to propagation through brain tissue is mainly due to dispersion of water, since brain tissue is over 75% water. Our calculation shows that, after 2-mm of water (i.e., the working distance of our water immersion objective lens), the 79 fs pulse (originally chirped from 65 fs) will be further broadened to ~ 100 fs. The effective thickness of the water layer (i.e., the water immersion layer plus the thickness of the tissue) is essentially independent of the imaging depth, making the pulse width approximately constant over the entire imaging depth.

2.6 Methods: imaging setup

Imaging is performed with a multiphoton microscope [11,12] (Fig. 2.7). We use heavy water (D_2O), which is safe and widely available, instead of regular water as the immersion liquid in order to minimize the absorption of the 1,675 nm excitation by the liquid between the objective and the sample surface. The immersion D_2O is sealed from the moisture in the air because D_2O is hygroscopic. We use a photomultiplier tube (PMT) with a GaAsP photocathode (H7422-40, quantum efficiency (QE) at 600 nm $\sim 36\%$, Hamamatsu Photonics) to detect the fluorescence from Texas Red or RFP tdimer2(12). The filters are a 593-nm long-pass filter (Semrock) and a 630 ± 46 nm band-pass filter (Chroma Technology), respectively, for Texas Red and RFP tdimer2(12). The THG signal (558 nm) is detected through a 558 ± 10 nm band-pass

filter (Semrock) by an ultra bialkali PMT (R7600-200, QE at 560 nm ~10%, Hamamatsu Photonics). A movable objective microscope head (MOM, Sutter Instrument Company) translates the objective axially to change the imaging depth within the sample. The field of view (FOV) for each image is $123 \mu\text{m} \times 123 \mu\text{m}$. A computer running the ScanImage [29] module with MATLAB (Mathworks) software controls translation of the objective and the image acquisition. Current generated by the PMT is converted to voltage ($0.1 \text{ V}/\mu\text{A}$) and low-pass filtered (20 KHz) by a transimpedance amplifier (C7319, Hamamatsu Photonics). Analogue-to-digital conversion is performed by a data acquisition card (NI PCI-6110, National Instruments) at a sampling rate up to 5 million samples per second. Due to the low repetition rate of the laser (1 MHz), the pixel clock is roughly 15 microseconds, resulting in oversampling by our data acquisition card. For depth measurement, the slightly larger index of refraction in brain tissue (1.35 to 1.4 for the cortex [30,31] and as high as 1.467 for the white matter [31]), relative to water (~ 1.33), results in a slight underestimate (5–10%) of the actual imaging depth within the tissue because the imaging depths reported here are the raw axial movement of the objective. For image processing, a median filter with a 1 pixel radius was applied.

For *in vivo* axial resolution measurements, we drew a line across the capillary vessels in the fast scanning direction, and measured the maximum brightness along this line at each depth to get the axial brightness profile. This approach partially mitigates the motion artefacts caused by heartbeat and breathing, and avoids the dark pixels inside the capillary vessel caused by the non-labelled blood cells.

2.7 *Methods: animal procedures*

Animal procedures were reviewed and approved by the Cornell Institutional Animal Care and Use Committee. We used male FVB/N mice (23 g, 10 weeks old, Charles River) for Texas Red-labelled vasculature imaging, and B6.Cg-Tg(Thy1-Brainbow1.0)HLich/J mice (18 g, 6 weeks old, The Jackson Laboratory) for RFP-labelled neuron imaging. Animals were prepared using the methods described by Kobat [12]; the craniotomies were performed centred at 2 mm posterior and 2 mm lateral to the Bregma point. Prior to imaging the FVB/n mice, 200 µl of 70 kDa Texas Red-Dextran (Invitrogen, dissolved at 5% w/v in saline) was retro-orbitally injected to label the vasculature. The B6.Cg-Tg(Thy1-Brainbow1.0)HLich/J mice were not subjected to Cre recombinase, thus the only fluorescent protein expression was from RFP tdimer2(12).

2.8 *Methods: Perfusion and slicing.*

Mice (B6.Cg-Tg(Thy1-Brainbow1.0)HLich/J) were euthanized and perfused. Brain slices were prepared and imaged using the post-mortem histology methods described by Rosidi [32].

2.9 Supplementary data: comparing SBRs in 2PM and 3PM

We derive approximate expressions for SBRs in 2PM and 3PM. Our derivations assume that the imaging depth (z) is much greater than the tissue effective attenuation length (l_e), and l_e is much greater than the focal depth of the imaging system. These conditions are generally valid for high resolution imaging deep into scattering tissues. We further assume that the volume fraction that is labelled is one. For situations where the labelling is non-uniform and only a small fraction of the total volume (V_s/V) is labelled, the actual SBR needs to be scaled by approximately a factor of V/V_s [10].

The signal generated by a diffraction-limited beam in scattering media for 2PM is approximately [33]

$$\langle F(t)_{2P} \rangle = 8C_2 n_0 \frac{\langle P \rangle^2}{\pi \lambda} e^{-\frac{2z}{l_e}}, \quad (1)$$

while that of 3PM is [34]

$$\langle F(t)_{3P} \rangle = 3.5C_3 n_0 \frac{(NA)^2 \langle P \rangle^3}{\lambda^3} e^{-\frac{3z}{l_e}}, \quad (2)$$

where NA is the numerical aperture of the focusing lens, n_0 is the index of refraction of the imaging medium, $\langle P \rangle$ is the time-averaged power of the excitation beam, λ is the excitation wavelength, and z is the imaging depth in the tissue. C_2 and C_3 are constants that include the contributions such as the concentration of the dye, absorption cross section, etc.

The background is generated mainly within one effective attenuation length of the sample surface, and is given by,

$$B_n \propto \langle I \rangle^n A l_e = \frac{\langle P \rangle^n}{A^{n-1}} l_e, \quad (3)$$

where n is the photon order, $\langle I \rangle$ is the time-averaged intensity of the excitation beam, and A is the area of the excitation beam on the tissue surface. The 2PM background is

$$B_2 \approx C_2 \langle P \rangle^2 \frac{n_0^2 l_e}{\pi z^2 NA^2} \quad (4)$$

and the 3PM background is

$$B_3 \approx C_3 \langle P \rangle^3 \frac{n_0^4 l_e}{\pi^2 z^4 NA^4}. \quad (5)$$

Therefore, the 2PM SBR is

$$SBR_{2P} \approx \frac{6(NA)^2 z^2}{\lambda l_e} e^{-\frac{2z}{l_e}} \quad (6)$$

and the 3PM SBR is

$$SBR_{3P} \approx \frac{14.7z^4(NA)^6}{\lambda^3 l_e} e^{-\frac{3z}{l_e}}. \quad (7)$$

Equation (6) is in agreement with previous calculation for SBR in 2PM [10]. Fig. 2.6 compares the 2PM SBR with 1,280 nm excitation ($l_e = 285 \mu\text{m}$), 3PM SBR with 1,280 nm excitation ($l_e = 285 \mu\text{m}$), and 3PM SBR with 1,700 nm excitation ($l_e = 400 \mu\text{m}$). It is clear that 3PM imaging provides a significant improvement in SBR over 2PM, even when equal effective attenuation lengths are considered.

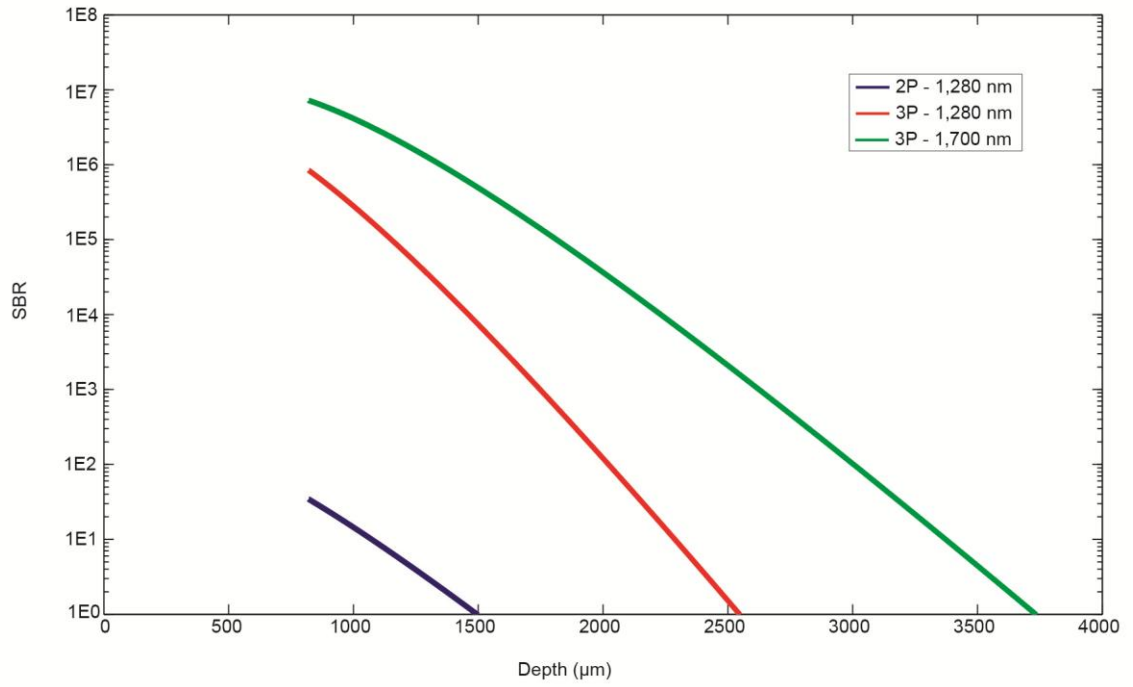


Figure 2.6: comparing SBRs in 2PM and 3PM. Calculated SBRs of 2PM and 3PM at $NA = 1$. The effective attenuation lengths are 285 μm and 400 μm for excitation at 1,280 nm and 1,700 nm, respectively.

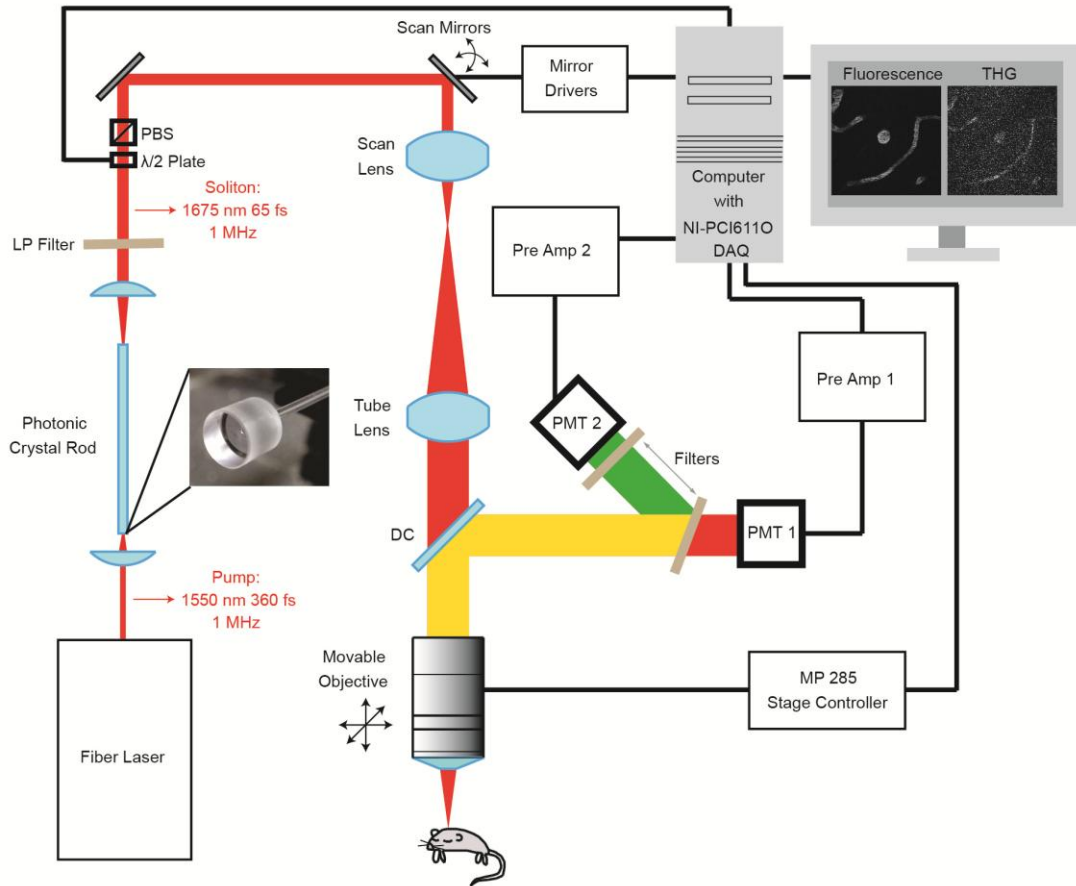


Figure 2.7: 3PM experimental setup. Schematic of the imaging setup. PBS: polarization beam splitter, DC: dichroic mirror, PMT: photomultiplier tube, $\lambda/2$ Plate: half wave plate, LP Filter: 1,600 nm long-pass filter. The excitation beam is raster-scanned by two galvanometer-driven mirrors (6215H, Cambridge Technology). Scan mirrors are imaged onto the back aperture of the microscope objective with a magnification of 6 times via a scan lens and a tube lens. The scan lens is a C-coated achromat (AC254-030-C-ML, Thorlabs) for high transmission (97%) at 1,675 nm, and the transmission of the tube lens (Sutter Instrument) is 82%. We use a custom high NA water immersion microscope objective (XLPlan N, Olympus, 25×1.05 NA), which is specially coated for high transmission (83%) at 1,675nm, to focus the excitation beam into the sample and to epi-collect the fluorescence and third harmonic signals. Epi-collected fluorescence and third harmonic signals are directed to the PMTs by the DC (750DCXXR, Chroma Technology). The power at the sample surface is adjusted by the $\lambda/2$ Plate (AQWP05M-1600, Thorlabs) and the PBS (PBS054, Thorlabs).

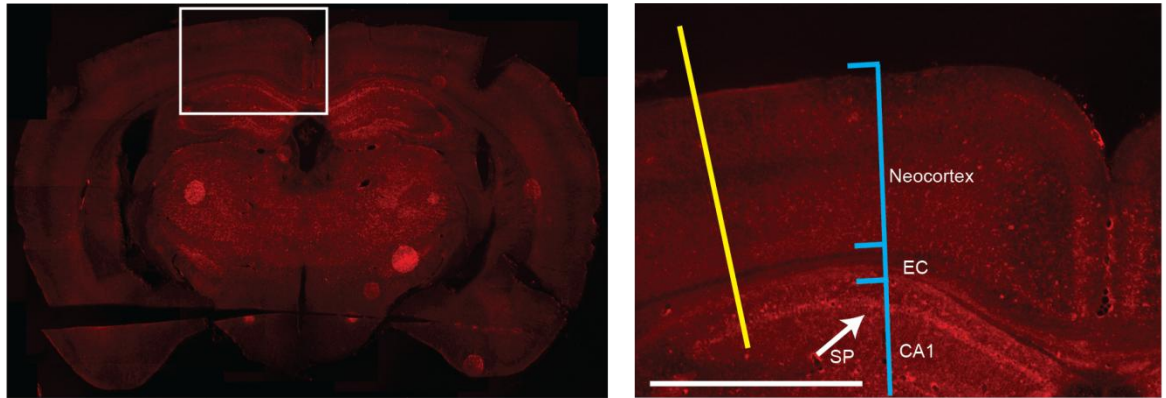


Figure 2.8: Epifluorescence images of the B6.Cg-Tg(Thy1 Brainbow1.0)HLich/J mouse brain. Left: Coronal section of the mouse brain, 2 mm caudal to bregma. The bright circles in the lower half of this frame are artefacts from the slide mounting process. Right: Zoomed-in region. The yellow line indicates the approximate location where 3PM imaging was performed, and the white arrow indicates the location of the SP. The scale bar is 1 mm.

2.10 Acknowledgments

This work is partially funded by grants from the National Institutes of Health (NIH) (R01CA133148), (R01EB014873), and (R21RR032392). N.G.H. is supported by the National Science Foundation, Graduate Research Fellowship Program (DGE-0707428). We acknowledge discussions with D. Dombeck, as well as N. Nishimura and J. Rubin for preparation of the *ex vivo* brain slices.

REFERENCES

1. Denk, W., Strickler, J.H. & Webb, W.W. Two-photon laser scanning fluorescence microscopy. *Science* **248**, 73-76 (1990).
2. Kerr, J.N.D. & Denk, W. Imaging in vivo: watching the brain in action. *Nat. Rev. Neurosci.* **9**, 195-205 (2008).
3. Dombeck, D.A., Harvey, C.D., Tian, L., Looger, L.L. & Tank, D.W. Functional imaging of hippocampal place cells at cellular resolution during virtual navigation. *Nat. Neurosci.* **13**, 1433-1440 (2010).
4. Olivier, N. *et al.* Cell lineage reconstruction of early zebrafish embryos using label-free nonlinear microscopy. *Science* **329**, 967-971 (2010).
5. Williams, R.M. *et al.* Strategies for high-resolution imaging of epithelial ovarian cancer by laparoscopic nonlinear microscopy. *Transl. Oncol.* **3**, 181-194 (2010).
6. Jung, J.C., Mehta, A.D., Aksay, E., Stepnoski, R. & Schnitzer, M.J. In vivo mammalian brain imaging using one- and two-photon fluorescence microendoscopy. *J. Neurophysiol.* **92**, 3121-3133 (2004).
7. Levene, M.J., Dombeck, D.A., Kasischke, K.A., Molloy, R.P. & Webb, W.W. In vivo multiphoton microscopy of deep brain tissue. *J. Neurophysiol.* **91**, 1908-1912 (2004).
8. Kleinfeld, D., Mitra, P.P., Helmchen, F. & Denk, W. Fluctuations and stimulus induced changes in blood flow observed in individual capillaries in layers 2 through 4 of rat neocortex. *Proc. Natl. Acad. Sci. U. S. A.* **95**, 15741-15746 (1998).

9. Svoboda, K., Helmchen, F., Denk, W. & Tank, D.W. Spread of dendritic excitation in layer 2/3 pyramidal neurons in rat barrel cortex in vivo. *Nat. Neurosci.* **2**, 65-73 (1999).
10. Theer, P., Hasan, M.T. & Denk, W. Two-photon imaging to a depth of 1000 μm in living brains by use of a Ti:Al₂O₃ regenerative amplifier. *Opt. Lett.* **28**, 1022-1024 (2003).
11. Kobat, D. *et al.* Deep tissue multiphoton microscopy using longer wavelength excitation. *Opt. Express* **17**, 13354-13364 (2009).
12. Kobat, D., Horton, N.G. & Xu, C. In vivo two-photon microscopy to 1.6-mm depth in mouse cortex. *J. Biomed. Opt.* **16**, 106014 (2011).
13. Helmchen, F. & Denk, W. Deep tissue two-photon microscopy. *Nat. Methods* **2**, 932-940 (2005).
14. Balu, M. *et al.* Effect of excitation wavelength on penetration depth in nonlinear optical microscopy of turbid media. *J. Biomed. Opt.* **14**, 010508 (2009).
15. Sacks, Z.S., Kurtz, R., Juhasz, T., Spooner, G. & Mourou, G.A. Subsurface Photodisruption in Human Sclera: Wavelength Dependence. *Ophthalmic Surg. Lasers Imaging* **34**, 104-113 (2003).
16. Kou, L., Labrie, D. & Chylek, P. Refractive indices of water and ice in the 0.65- to 2.5- μm spectral range. *Appl. Opt.* **32**, 3531-3540 (1993).
17. Xu, C., Zipfel, W., Shear, J.B., Williams, R.M. & Webb, W.W. Multiphoton fluorescence excitation: new spectral windows for biological nonlinear microscopy. *Proc. Natl. Acad. Sci. U. S. A.* **93**, 10763-10768 (1996).

18. Hell, S.W. *et al.* Three-photon excitation in fluorescence microscopy. *J. Biomed. Opt.* **1**, 71-74 (1996).
19. Wokosin, D.L., Centonze, V.E., Crittenden, S. & White, J. Three-photon excitation fluorescence imaging of biological specimens using an all-solid-state laser. *Bioimaging* **4**, 208-214 (1996).
20. Zysset, B., Beaud, P. & Hodel, W. Generation of optical solitons in the wavelength region 1.37–1.49 μm . *Appl. Phys. Lett.* **50**, 1027-1029 (1987).
21. Wang, K. & Xu, C. Tunable high-energy soliton pulse generation from a large-mode-area fiber and its application to third harmonic generation microscopy. *Appl. Phys. Lett.* **99**, 071112 (2011).
22. Limpert, J. *et al.* High-power rod-type photonic crystal fiber laser. *Opt. Express* **13**, 1055-1058 (2005).
23. Barad, Y., Eisenberg, H., Horowitz, M. & Silberberg, Y. Nonlinear scanning laser microscopy by third harmonic generation. *Appl. Phys. Lett.* **70**, 922-924 (1997).
24. Müller, M., Squier, J., Wilson, K.R. & Brakenhoff, G.J. 3D microscopy of transparent objects using third-harmonic generation. *J. Microsc.* **191**, 266-274 (1998).
25. Farrar, M.J., Wise, F.W., Fetcho, J.R. & Schaffer, C.B. In vivo imaging of myelin in the vertebrate central nervous system using third harmonic generation microscopy. *Biophys. J.* **100**, 1362-1371 (2011).
26. Livet, J. *et al.* Transgenic strategies for combinatorial expression of fluorescent proteins in the nervous system. *Nature* **450**, 56-62 (2007).

27. Franklin, K.B.J. & Paxinos, G. *Mouse brain in stereotaxic coordinates*. (Academic Press, London, 2008).
28. Murphy, P. A et al. Notch4 normalization reduces blood vessel size in arteriovenous malformations. *Sci. Transl. Med.* **4**, 117ra8 (2012).
29. Pologruto, T.A., Sabatini, B.L. & Svoboda, K. ScanImage: flexible software for operating laser scanning microscopes. *Biomed. Eng. Online* **2**, 13 (2003).
30. Binding, J. et al. Brain refractive index measured in vivo with high-NA defocus corrected full-field OCT and consequences for two-photon microscopy. *Opt. Express* **19**, 4833-4847 (2011).
31. Bacallao, R., Sohrab, S. & Phillips, C. Guiding Principles of Specimen Preservation for Confocal Fluorescence Microscopy, *In Handbook Of Biological Confocal Microscopy* (Ed, Pawley, J.B.), 368-380.
32. Rosidi, N.L. et al. Cortical microhemorrhages cause local inflammation but do not trigger widespread dendrite degeneration. *Plos One* **6**, e26612 (2011).
33. Xu, C. & Webb, W.W. Measurement of two-photon excitation cross sections of molecular fluorophores with data from 690 to 1050 nm. *J. Opt. Soc. Am. B* **13**, 481-491 (1996).
34. Xu, C. & Webb, W. W. Multiphoton excitation of molecular fluorophores and nonlinear laser microscopy, *In Topics in fluorescence spectroscopy*, Vol. 5 (Ed, Lakowicz, J. R.), 471-540.

CHAPTER 3

DISPERSION COMPENSATION IN THREE-PHOTON FLUORESCENCE MICROSCOPY AT 1,700 NM²

3.1 *Abstract:*

Signal generation in three-photon microscopy is proportional to the inverse-squared of the pulse width. Group velocity dispersion is anomalous for water as well as many glasses near the 1,700 nm excitation window, which makes dispersion compensation using glass prism pairs impractical. We show that the high normal dispersion of a silicon wafer can be conveniently used to compensate the dispersion of a 1,700 nm excitation three-photon microscope. We achieved over a factor of two reduction in pulse width at the sample, which corresponded to over a 4x increase in the generated three-photon signal. This signal increase was demonstrated during *in vivo* experiments near the surface of the mouse brain as well as 900 μm below the surface.

3.2 *Introduction*

Dispersion management is critical for multiphoton microscopy because ultrashort pulses can be strongly affected by material dispersion [1], which results in reduced signal generation. Dispersion management components are common in two-photon microscopy (2PM) systems [2,3], and 2PM systems have been shown to

² The contents of this chapter have been reproduced from Biomedical Optics Express 6(4), 1392-1397 (2015).

maintain a laser pulsewidth down to 10 fs [4]. However, glasses commonly used in a microscope generate normal material group velocity dispersion (GVD) at the typical excitation wavelengths for 2PM (600-1300 nm) and can thus be compensated by prism pairs [1-6], which are capable of generating significant anomalous GVD. For example, commercial devices such as the DeepSee (Newport) are capable of introducing -40,000 fs² of (anomalous) GVD at 690 nm and -8,000 fs² of GVD at 1,300 nm, which are generally sufficient for most microscopes at these wavelengths.

Three-photon microscopy (3PM) using 1,700 nm excitation wavelength was recently shown to produce images within *in vivo* brain tissue at unprecedented depths due to the higher order of nonlinearity and longer excitation wavelength than traditional 2PM [7]. The inverse-squared relationship between the generated signal and the duty cycle of the pulse train for 3PM, as opposed to the simple inverse relationship for 2PM [8,9], necessitates the use of short (<70 fs), energetic (~100 nJ) excitation pulses. However, the GVD is anomalous for many glasses commonly used in microscopes at this wavelength, and a net anomalous GVD makes the use of typical glass prism pairs impractical for dispersion compensation. In addition, the immersion liquid (e.g., H₂O and D₂O), and perhaps the brain tissue itself, can introduce anomalous dispersion and must also be considered.

Fig. 3.1 shows the GVD of various optical materials as calculated from their Sellmeier equations [10–14]. The GVD curves of H₂O and D₂O only extend to 1.6 μm because the Sellmeier coefficients in reference [14] were shown to match experiments to this wavelength. H₂O and D₂O as well as common types of glasses such as fused silica and N-LAK22 exhibit anomalous dispersion near 1,700 nm. However, the strong

normal dispersion of silicon (Si) means that anomalous dispersion can be compensated by merely inserting a Si wafer into the beam path. Furthermore, the beam shouldn't suffer any transmission loss through the wafer if the wafer is undoped and uncoated as well as positioned at the Brewster angle, which is approximately at a 74 degree angle of incidence, and the incident light is p-polarized.

Second order autocorrelations were performed to measure how the laser pulse broadens after traveling through combinations of water (H₂O), heavy water (D₂O), Si, and the microscope. Fig. 3.2 shows the experimental setup. The laser and PC rod combination produces a pulse of light centered at 1,700 nm with a 53 fs full-width at half maximum (FWHM). This initial pulse was measured by a second-order interferometric autocorrelator. After the interferometer, the light can pass through a variety of dispersive elements (1 mm cuvette filled with H₂O, 1 cm cuvette filled with D₂O, Si wafers of various thicknesses, and the microscope optics). Each sidewall of the cuvette is made of 1.25-mm thick fused silica, so each cuvette introduces approximately -100 fs² group delay dispersion (GDD). To achieve a 2 mm path length through H₂O, the incident light is double-passed through the 1-mm cuvette. A Si detector (SM05PD1A, Thorlabs) at the "Sample" position serves as the nonlinear element and produces a 2-photon induced current that is converted to voltage by a transimpedance amplifier (SR570, Stanford Research Systems) and then recorded by a computer.

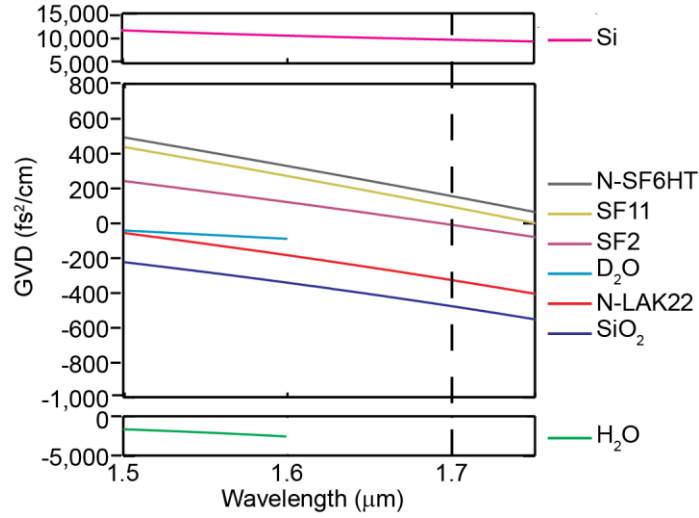


Fig. 3.1: Material GVD vs. wavelength near 1,700 nm for common optical materials. The vertical line at 1.7 μm denotes our excitation wavelength. Note the different scales used for Si and H_2O .

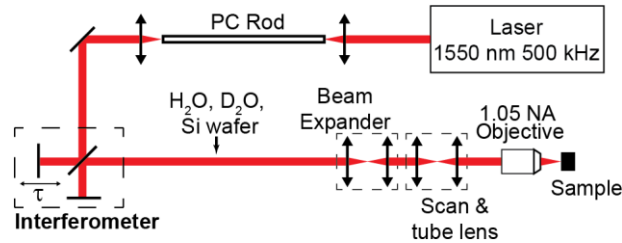


Fig. 3.2: Experimental setup. The PC Rod shifts the wavelength of the laser from 1.55 μm to 1.7 μm through soliton self-frequency shift [7]. Dispersive elements (H_2O , D_2O , microscope optics, and Si wafers) were independently added to the beam path.

Fig. 3.3 shows the pulse spectrum and 2nd-order interferometric autocorrelations of our experiment. The numbers in the upper-right corner of Fig. 3.3(b-h) are the intensity FWHM of each pulse (after deconvolution by assuming a sech^2 pulse shape). The dispersion introduced by 2 mm H_2O (Fig. 3.3(b)), which is the working distance of our objective, is nearly identical to that of 1 cm D_2O (Fig 3.3(c)). We use D_2O as our 3PM immersion fluid because it has a similar linear index of

refraction as H_2O but significantly lower absorption [14]. The small GVD that we observed from D_2O , which is corroborated by the calculated dispersion shown in Fig. 3.1, allows us to neglect its impact for 3PM since less than 2-mm thick D_2O is present in any imaging conditions. The thickness of the brain tissue in our experiments may also introduce extra dispersion. Since water content of brain tissue is approximately 80% [15], we performed our experiments with 1- and 2-mm H_2O together with our microscope. We found a 3-mm Si wafer is near the ideal thickness for our system (Figs. 3.3f and 3.3h). It is shown that the pulsewidth is compressed by over a factor of 2 after the 3-mm Si wafer, which should result in over a fourfold increase in the 3-photon excited signal.

We performed *in vivo* imaging to show how the introduction of the Si wafer will increase the 3-photon excited signal for the same input beam. The microscope setup was similar to that shown in Horton et al. [7], with the exception of a PC rod with a larger core area that produces a soliton with roughly twice the pulse energy of the initial system [16].

We placed the 3 mm Si wafer (Edmund Optics) at the Brewster angle in order to minimize power loss. Transmitted power was measured after the microscope objective both before and after insertion of the wafer. No difference in the measured power was observed. The Brewster angle incidence increases the optical path length through the Si by approximately 4% of the wafer thickness.

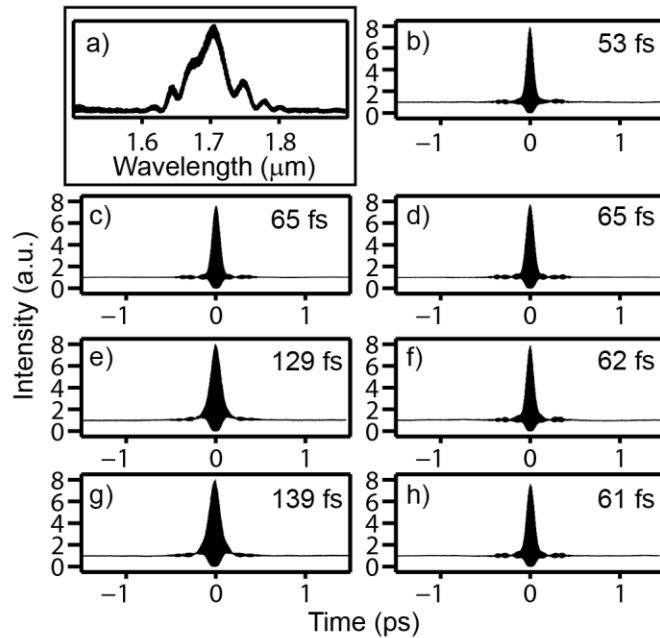


Fig. 3.3: Spectrum of pulse and second-order interferometric autocorrelations after various optical elements. (a) Pulse spectrum after the PC rod. (b)-(h) Second-order interferometric autocorrelations: (b) immediately after the collimating lens following the PC rod, (c) after 2 mm H_2O , (d) after 1 cm D_2O , (e) after microscope and 1 mm H_2O , (f) after microscope, 1 mm H_2O , and 3 mm Si, (g) after microscope and 2 mm H_2O , (h) after microscope, 2 mm H_2O , and 3 mm Si. The intensity FWHM of the pulse, assuming a sech^2 pulse, is also displayed in each panel.

Fig. 3.4 shows the results of *in vivo* experiments recorded on the mouse brain. The mouse was prepared similar to that described in Horton et al. [7]. We used D_2O as the immersion fluid because it has much lower absorption than that of H_2O at 1,700 nm. The power at the surface was 1.4 mW when imaging 50 μm below the surface and 25 mW when imaging 900 μm below the surface. Deeper imaging was possible, but the depth at 900 μm was chosen because a large vessel provided a good measure for brightness comparison. Each depth shows approximately 4x increase in signal using the Si wafer, which agrees well with our pulse width measurements. It is important to

note that the relative signal increase was similar at each depth despite different amounts of D₂O and brain tissue involved. Our results indicate that fine-tuning the Si thickness at different imaging depth is unnecessary when imaging down to approximately 1 mm depth in a mouse brain using a 53 fs pulse at 1,700 nm.

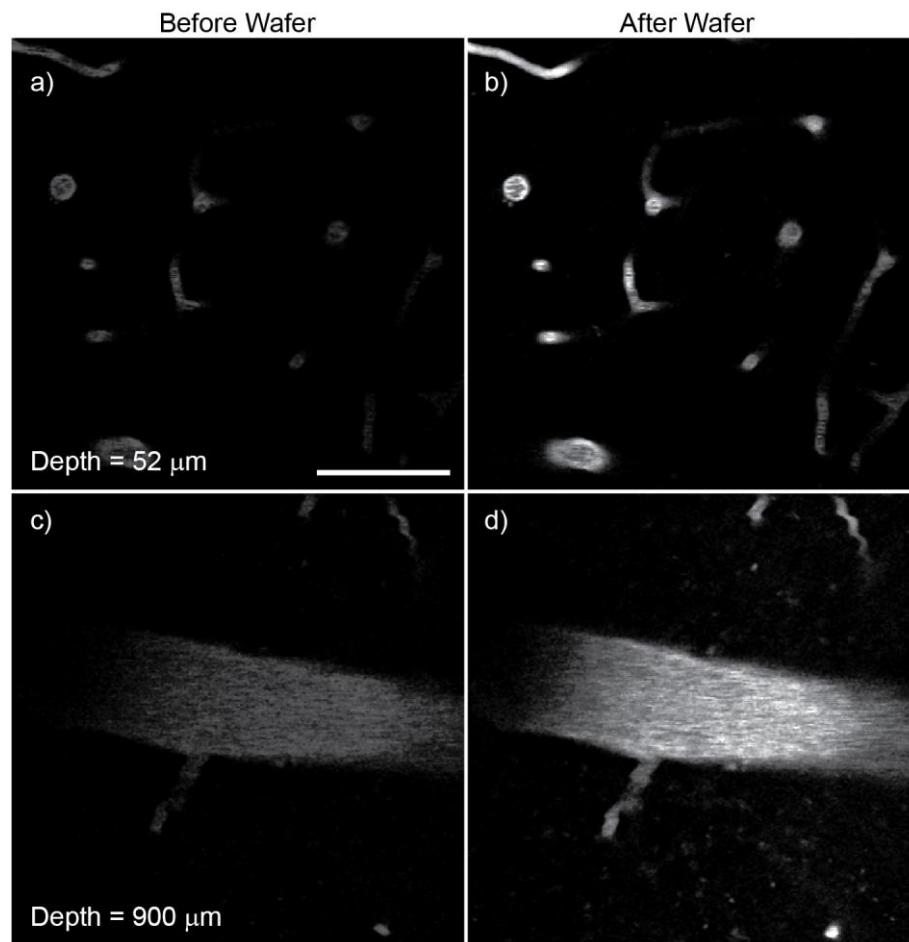


Fig. 3.4: In vivo three-photon microscopy of Texas Red-labeled blood vessel within an intact mouse brain. (a) and (c) were recorded without the Si wafer, while (b) and (d) were recorded after insertion of the 3 mm wafer at the Brewster angle. The brightness of the images reflects the signal level. Scale bar, 50 μm .

3.3 Discussion

We showed that the simple introduction of a Si wafer resulted in a 4x improvement of 3-photon excited signal for our three-photon microscope. Although fine-tuning the GDD is possible using Si prisms [6,17,18], adding a Si wafer to the optical beam path is significantly simpler. Since Si wafers of various thicknesses are readily available commercially, the addition of the Si wafer provides a simple, practical solution for dispersion compensation at 1,700 nm.

We were able to compress the pulse after the microscope to approximately 115% of the original pulse width using Si wafers at 0.5 mm thickness increments. The discrete nature of our dispersion compensation may introduce a maximum residual GDD of approximately 250 fs^2 , which can account for a fraction of the residual broadening (for example, we predict that 250 fs^2 will broaden the pulse by ~9% (~58 fs vs. ~53 fs). Pulse broadening due to third order dispersion (TOD) is a concern at 1,700 nm. TOD for common optical materials is displayed in Fig. 3.5. TOD is positive at 1,700 nm for many common glasses as well as Si, which means that Si cannot provide TOD compensation. Theoretical analysis shows that TOD of $30,000 \text{ fs}^3$ will cause a 15% increase in minimum pulsewidth for a 53 fs pulse. It is interesting to note that many types of glasses have between 2000 to $2800 \text{ fs}^3/\text{cm}$ TOD (Fig. 3.5 and Table 3.1). Our imaging system includes approximately 12 cm of glass. Even though the exact types of glasses used in the microscope optics are not known, it is plausible that TOD could account for a fraction or all of the 15% minimum pulse width increase.

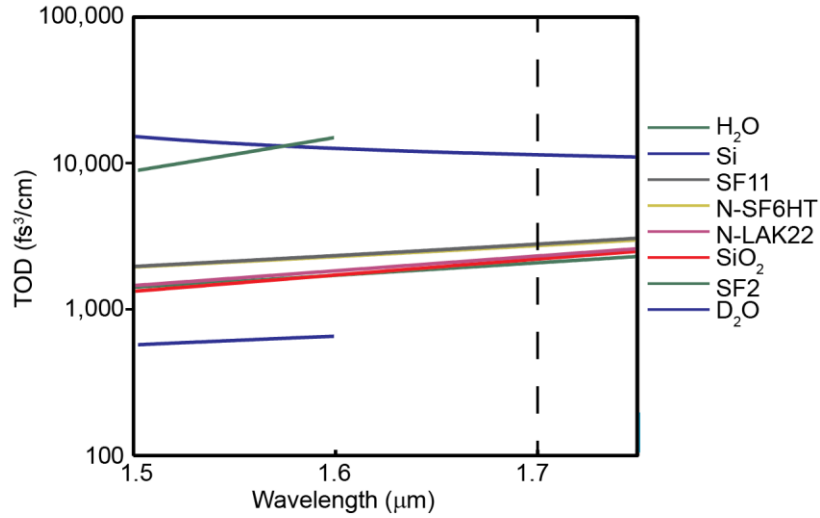


Fig. 3.5: TOD of common optical materials.

Table 3.1. Calculated GVD and TOD of various materials at 1,700 nm. The bold values are calculations at 1,600 nm

Material	<i>GVD</i> (<i>fs</i> ² / <i>cm</i>)	<i>TOD</i> (<i>fs</i> ³ / <i>cm</i>)
H₂O	-2,525	14,932
Si	9,827	11,406
SF11	95	2,795
N-SF6HT	156	2,727
N-LAK22	-326	2,317
NBK7	-448	2,261
Fused Silica	-475	2,206
SF2	-9	2,082
D₂O	-89	660

In summary, we show that a Si wafer of appropriately chosen thickness can conveniently compensate for the anomalous dispersion introduced by the optical components in a three-photon microscope at 1,700 nm. A factor of over two pulsewidth reduction at the sample is obtained by the simple addition of a 3-mm Si wafer at Brewster angle incidence, which leads to a factor of 4 improvement in signal for three-photon *in vivo* imaging. Our results further indicate that fine-tuning the Si

thickness is unnecessary as a function of imaging depth when imaging down to approximately 1 mm depth in a mouse brain using a 53 fs pulse at 1,700 nm. Finally, TOD generated by glass optics and H₂O may be a concern at 1,700 nm, particularly if a pulse width much shorter than 50 fs is used.

3.4 *Acknowledgments:*

This paper was partially supported by The National Institutes of Health (R01EB014873). The authors would like to thank Dimitre Ouzounov, David Sinefeld, and Kriti Charan for helpful discussions with the experiment.

REFERENCES

1. I. Walmsley, L. Waxer, and C. Dorrer, "The role of dispersion in ultrafast optics," *Rev. Sci. Instrum.* **72**(1), 1-29 (2001).
2. D. Entenberg, J. Wyckoff, B. Gligorijevic, E. T. Roussos, V. V. Verkhusha, J. W. Pollard, and J. Condeelis, "Setup and use of a two-laser multiphoton microscope for multichannel intravital fluorescence imaging," *Nat. Protoc.* **6**(10), 1500-1520 (2011).
3. M. Müller, J. Squier, R. Wolleschensky, U. Simon, and G. J. Brakenhoff, "Dispersion pre-compensation of 15 femtosecond optical pulses for high-numerical-aperture objectives," *J. Microsc.* **191**(2), 141-150 (1998).
4. P. Xi, Y. Andegeko, L. R. Weisel, V. V. Lozovoy, and M. Dantus, "Greater signal, increased depth, and less photobleaching in two-photon microscopy with 10 fs pulses," *Opt. Commun.* **281**(7), 1841-1849 (2008).
5. R. L. Fork, O. E. Martinez, and J. P. Gordon, "Negative dispersion using pairs of prisms," *Opt. Lett.* **9**(5), 150-152 (1984).
6. R. E. Sherriff, "Analytic expressions for group-delay dispersion and cubic dispersion in arbitrary prism sequences," *J. Opt. Soc. Am. B* **15**(3), 1224-1230 (1998).
7. N. G. Horton, K. Wang, D. Kobat, C. G. Clark, F. W. Wise, C. B. Schaffer, and C. Xu, "In vivo three-photon microscopy of subcortical structures within an intact mouse brain," *Nat. Photonics* **7**(3), 205-209 (2013).

8. C. Xu and W. W. Webb, "Multiphoton excitation of molecular fluorophores and nonlinear laser microscopy," in *Topics in Fluorescence Spectroscopy*, J. R. Lakowicz, ed. (Plenum, 1997), Vol. 5, pp. 471-540.
9. B. Nie, I. Saytashev, A. Chong, H. Liu, S. N. Arhipov, F. W. Wise, and M. Dantus, "Multimodal microscopy with sub-30 fs Yb fiber laser oscillator," *Biomed. Opt. Exp.* **3**(7), 1750-1756 (2012).
10. G. P. Agrawal, *Nonlinear Fiber Optics* (Academic, 2001).
11. C. D. Salzberg and J. J. Villa, "Infrared refractive indexes of silicon germanium and modified selenium glass," *J. Opt. Soc. Am.* **47**(3), 244-246 (1957).
12. I. H. Malitson, "Interspecimen comparison of the refractive index of fused silica," *J. Opt. Soc. Am.* **55**(10), 1205-1209 (1965).
13. "Schott optical glass data sheets,"
http://www.schott.com/advanced_optics/us/abbe_datasheets/schott_datasheet_all_us.pdf
14. S. Kedenburg, M. Vieweg, T. Gissibl, and H. Giessen, "Linear refractive index and absorption measurements of nonlinear optical liquids in the visible and near-infrared spectral region," *Opt. Mat. Exp.* **2**(11), 1588-1611 (2012).
15. H. C. Agrawal, J. M. Davis, and W. A. Himwich, "Developmental changes in mouse brain: weight, water content and free amino acids," *J. Neurochem.* **15**(9), 917-923 (1968).
16. K. Wang, N. G. Horton, K. Charan, and C. Xu, "Advanced fiber soliton sources for nonlinear deep tissue imaging in biophotonics," *IEEE J. Sel. Top.*

Quant. Elect. **20**(2), 6800311 (2014).

17. C. Erny, C. Heese, M. Haag, and U. Keller, “High-repetition-rate optical parametric chirped-pulse amplifier producing 1- μ J, sub-100-fs pulses in the mid-infrared,” Opt. Exp. **17**(3), 1340-1345 (2009).
18. A. Sell, G. Krauss, R. Scheu, R. Huber, and A. Leitenstorfer, “8-fs pulses from a compact Er:fiber system: quantitative modeling and experimental implementation,” Opt. Exp. **17**(2), 1070-1077 (2009).

CHAPTER 4

IMAGING THE MOUSE BRAIN THROUGH AN UNTHINNED, INTACT SKULL USING THREE-PHOTON MICROSCOPY AT 1,700 NM EXCITATION

4.1 *Abstract*

Structural imaging of the mouse brain *in vivo* has been the focus of intense study in recent years. The strong scattering properties of the skull traditionally require either its partial or total removal in order to achieve significant depth penetration in the brain. This perturbation of the skull has been shown to alter the properties of the brain, which subsequently affects imaging experiments. In this article, we demonstrate *in vivo* vascular imaging 720 μm below the skull-brain interface of an unthinned, intact mouse skull, which is the deepest high-resolution through-skull imaging demonstrated to date. Red fluorescent protein-tagged neurons are also observed 350 μm below the skull-brain interface, which coincides with layer 2/3 of the neocortex.

4.2 *Introduction*

Studying the mouse brain is critical for understanding brain dynamics and disease progression. Significant progress has been made to develop mouse models, such as using neurotoxins or creating a genetically mutated colony, that can express a variety of characteristics ranging from fluorescent protein expression in neurons [1] to progression of conditions such as Alzheimer's Disease [2], Multiple Sclerosis [3], and Parkinson's Disease [4]. The mouse model is very useful for biologists who study a wide variety of brain dynamics, and adequate imaging technologies are necessary for

observing these dynamics *in vivo*.

The brain is a complicated organ, and minimal modification must be performed to ensure that *in vivo* imaging isn't modified by surgical preparation. This is especially challenging for high-resolution imaging techniques because their maximum penetration depth can be small. Fluorescence methods, such as confocal and two-photon microscopy, are widely used for structural and functional brain imaging with submicron resolution. However, because of their shallow penetration depth due to tissue scattering, modifications such as the removal of overlying skin, as well as the partial or complete removal of overlying skull bone ("skull thinning" and "craniotomy", for example), are usually required. Results show that a craniotomy can have a significant impact on glial activation relative to skull thinning [5], and the skull thinning process itself also produces mechanical stresses that can disrupt normal brain function [6].

Technologies such as magnetic resonance imaging [7] and photoacoustic tomography [8] have been able to produce images below an intact skull and scalp, which precludes any damage caused by surgical preparation. However, these technologies are incapable of single-cell resolution, which prevents its use for observing neuronal-scale events (i.e., action potentials, dendritic spine plasticity). Hong et al. recently presented the creation and use of carbon nanotube-based fluorophores for one-photon fluorescence imaging [9]. Fluorescence imaging with these molecules allow vascular imaging over 2 mm below the surface of the brain with a lateral resolution of approximately 10 μm . Further advancements with this technology, e.g., conjugation of an acetoxymethyl ester to the fluorophore [10], could

eventually allow *in vivo* imaging of neural clusters through the scalp with this technology; however, imaging a single axial plane is difficult with this technology.

High-resolution imaging, especially using previously developed genetically modified mouse models, has not been shown through an intact skull and scalp. The removal of the scalp, while maintaining the structure of the bone, is an alternative approach. Optical micro-angiography, a variation of optical coherence tomography (OCT), has been shown to image the mouse brain with the scalp removed but the skull intact [11,12]; however, the lateral resolution is greater than 12 μm , which is significantly larger than the ~ 3 μm diameter of the smallest capillaries [13]. Adaptive optics was recently used for two-photon fluorescence imaging roughly 120 μm through an intact skull [14], which is relatively shallow within the roughly 850 μm of the mouse neocortex. To date, no technology has been shown for 3d-resolved through-skull fluorescence imaging deep within the mouse cortex.

In this article, we present our use of three-photon fluorescence microscopy for brain imaging below an intact skull. Multiphoton microscopy was invented in the 1990s and allows sub- μm resolution while also imaging significantly deeper than traditional 1-photon techniques [15]. Two photon imaging has been shown to image through the entire cortical stack of the post-craniotomy mouse brain [16], but is limited by the signal-to-background ratio (SBR) at approximately 5-6 attenuation lengths within the tissue, which makes through-skull imaging impractical. Three-photon microscopy (3PM) imaging with 1,700 nm excitation wavelength was recently shown to produce hippocampal images within an *in vivo* mouse brain without the need of removing overlying tissue [17], but this experiment was also conducted after

performing a craniotomy.

Our experiments involved 3PM to perform *in vivo* imaging through the center of the parietal bone of an unthinned skull. Minimal preparation was performed prior to imaging (see Methods).

4.3 Results

Imaging beneath the mouse skull is difficult because the mouse skull induces wavefront aberrations as well as scattering. The mouse skull is heterogeneous, comprising of two layers of compact bone surrounding a region of cancellous bone (in certain instances, the two layers of compact bone can also fuse to form one layer) [18]. The bone thickness is also variable, and regions near the sutures are much thicker than in the center of the plate. In addition to this variation in thickness, bone possesses a high index of refraction (~ 1.55 at 589 nm [19]), which can further exacerbate wavefront aberrations caused by skull surface roughness. Therefore, it is plausible that signal generation could vary significantly for brain imaging at different locations on the skull. We determined the signal decay properties at multiple locations on a mouse skull by imaging brain vasculature labeled with dextran-conjugated Texas Red dye (see Methods). Figure 4.1a is a map that shows the imaging locations, while Figure 4.1b shows the signal decay curve, as a function of depth, for each location. The crosshair in Fig. 4.1a denotes the location roughly 2 mm caudal and 2 mm to the left relative to bregma. The depths labeled in Figure 4.1(b) are relative to the surface of the skull. The fluorescence signal at each of the imaging locations are within roughly 1 unit on the y-axis, which means that the brightest measured signal is usually less than

270% of the dimmest measured signal. Our results indicated that the imaging properties through the intact skull are reasonably uniform within the region investigated.

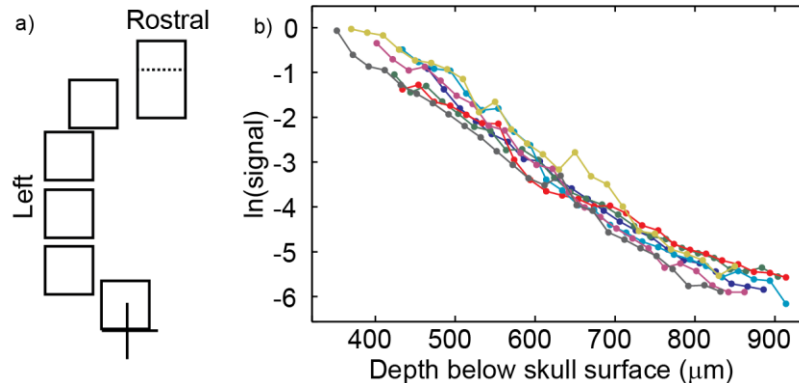


Figure 4.1: Through-skull imaging locations of a mouse with Texas-Red labeled vasculature. (a) Location map of where the imaging was performed. Field-of-views (i.e., each square) were $170 \times 170 \mu\text{m}$. The crosshair is positioned 2 mm left and 2 mm caudal relative to bregma. (b) Signal decay curves for each of the seven positions in (a). The depths are relative to the surface of the skull.

Figure 4.2 displays the results of a z-stack performed at one of the imaging locations from Figure 4.1(a). The first channel shows fluorescence from Texas Red-stained vasculature, while the second channel shows third harmonic generation (THG). Details about the image processing are described in Methods. The THG within the skull is predominantly from interfaces between osteocytes and surrounding bone matrix [20], and we did not identify any vasculature within the imaging region. The lack of vasculature is plausible since red (hematopoietic) marrow, which is heavily vascularized, is located exclusively near the central sinus of the adult mouse skull [21], while the center of the parietal bone in the adult mouse (i.e., our imaging region) contains either sparsely-vascularized yellow (fatty) marrow [22] or no marrow

due to the fusion of the compact bone plates [18]. No fluorescence was identified within the skull, and the THG features within the skull are significantly different than those in the brain; these characteristics allow clear demarcation of the skull-brain interface. Within the the brain, the fluorescence signal was significantly brighter than the THG; however, the THG signal from vasculature and myelinated axons were also visible.

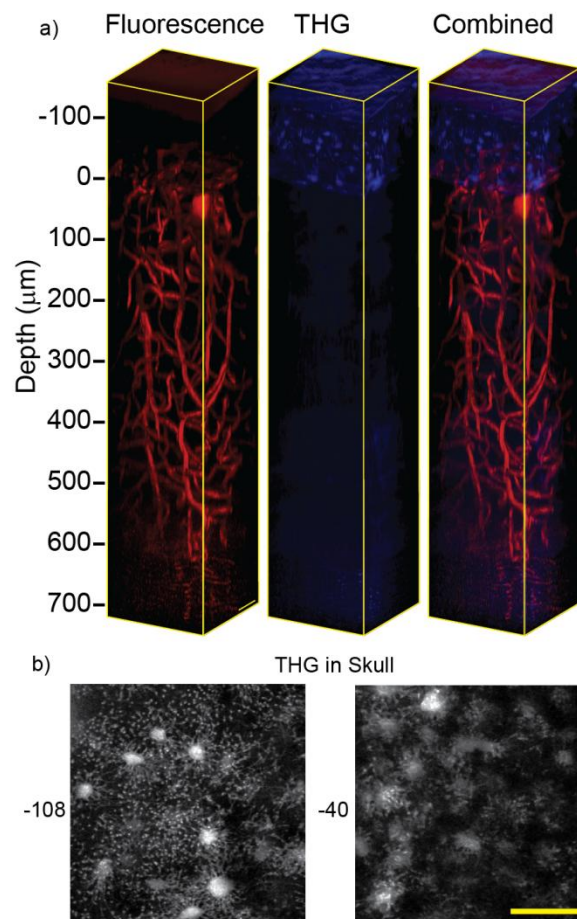


Fig. 4.2: a) Through-skull imaging of the vasculature of mouse brain. The skull-brain interface is observed by boundaries in the fluorescence and THG channels. (b): THG images within the mouse skull. Scale bars, 50 μm .

We also performed an experiment to compare the same imaging region of the

brain before and after craniotomy. Figure 4.3 shows our results. The black dots represent the THG signal generated within the skull, the blue dots represent the fluorescence generation in the brain through-skull, and the green dots represent the fluorescence generation post-craniotomy. While THG differs from fluorescence in that the signal is affected by scatterer size and beam profile [23], the THG curve can still be used as a rough guide to signal decay within the skull. Two interesting features are noticed in Fig. 4.3. First, the attenuation length for the through-skull imaging ($\sim 230 \mu\text{m}$) is significantly shorter than that post-craniotomy ($\sim 390 \mu\text{m}$). We suggest that as we image deeper within the mouse brain, the area of the excitation beam on the surface of the skull increases, which also increases the aberration effects from the skull. Second, it is interesting that the signal decay length for the blue curve (i.e., through skull) in the first $100 \mu\text{m}$ of the brain matches that of the skull (i.e., $\sim 77 \mu\text{m}$), but the green curve (i.e., post craniotomy) does not show a different slope for the first $100 \mu\text{m}$. This sharper decay within the first $100 \mu\text{m}$ of the brain is also visible in through-skull imaging of the brainbow mouse (Figure 4.8). With regard to the attenuation length of the skull, experiments were previously shown for *in vitro* porcine bone tissue at $1,700 \text{ nm}$ to be approximately $78 \mu\text{m}$ [24], although this value may differ from mouse skull *in vivo*.

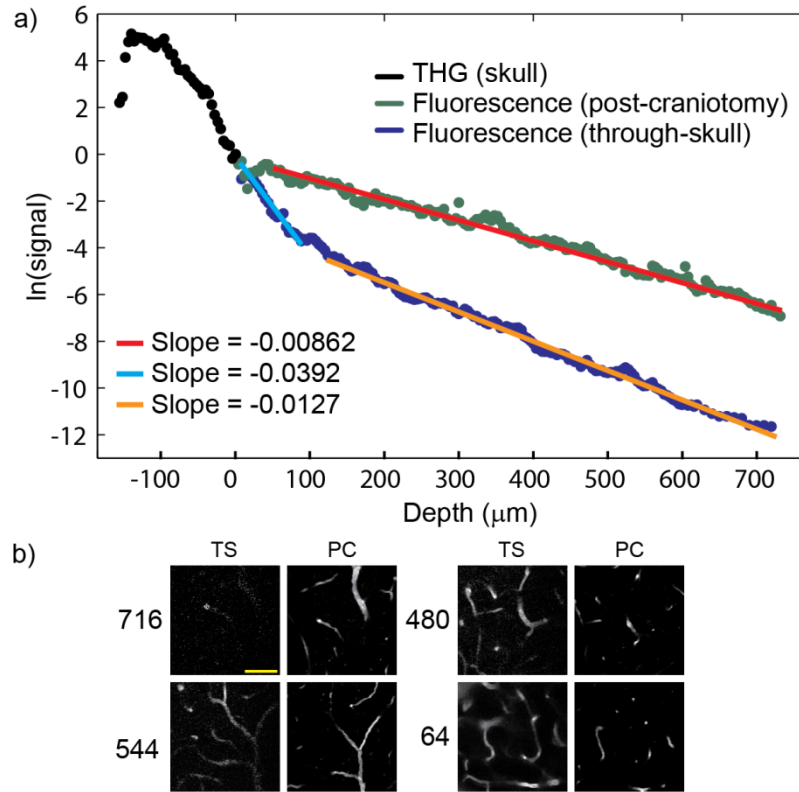


Fig. 4.3. Signal attenuation before and after craniotomy. (a) THG signal attenuation within the skull (black dots), fluorescence signal attenuation within the brain below the skull (blue dots), and fluorescence signal attenuation in the same region of the brain post-craniotomy (green dots). The curves were matched at depth = 0 (i.e., the skull-brain interface). The decay length of the brain, through-skull, was 236 μm , and the decay length post-craniotomy was 357 μm . Note that the slope of the THG curve is similar to that of the through-skull fluorescence for the first ~ 100 μm . (b) Comparison of through-skull (TS) and post-craniotomy (PC) frames for various depths below the brain surface.

Figure 4.3(b) shows comparison for through-skull imaging and post-craniotomy imaging at various depths. The numbers in each frame are the measured depths below the skull-brain interface, and the image frames obtained after craniotomy were chosen to match the major features of the through-skull images. There are noticeable differences in morphology between the through-skull images and the

images obtained after craniotomy. This is likely because the brain deformed when the cover glass was pressed on to it for post-craniotomy imaging. Features matched deep within the mouse brain were also identified roughly 20 μm deeper for through-skull imaging than for post-craniotomy, which can also be due to distortions from pressing the cover glass on the post-craniotomy brain surface.

Aberrations induced by through-skull imaging could have a significant effect on the resolution of the brain features. Figure 4.4 compares axial resolutions of blood vessels before and after craniotomy at different depths below the brain surface. The depths indicated represent the depth below the skull-brain interface for through-skull imaging, and the closest-matched craniotomy image was chosen as comparison. These numbers provide an “upper bound” for the microscope resolution [16]. There is a slight decrease in resolution 284 μm below the surface of the brain, which is likely due to wavefront aberrations induced by the presence of the skull. Figure 4.4 also shows a lateral profile for the through-skull imaging 718 μm below the skull-brain interface. The measured SBR was greater than 100, which indicates that SBR is not a limiting factor in 3PM through-skull imaging [17].

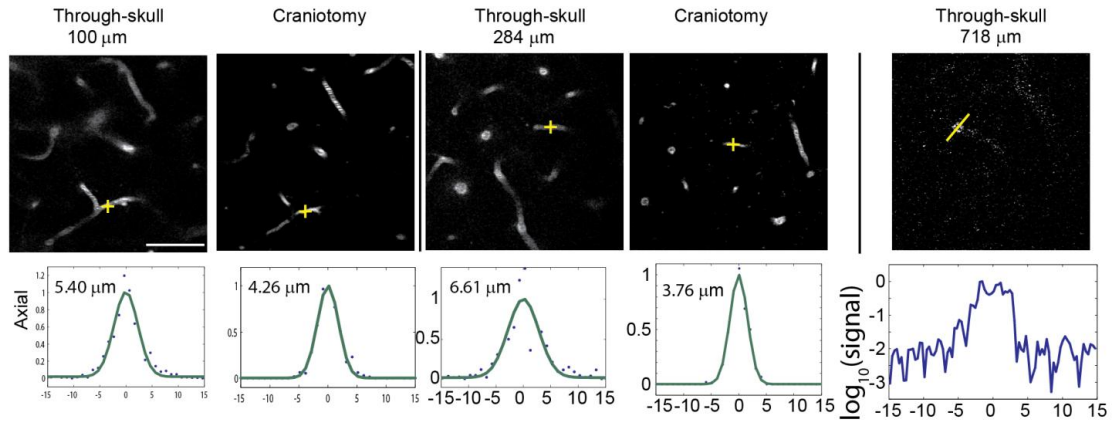


Figure 4.4: (a) Axial resolution comparisons of vascular imaging. The corresponding “craniotomy” images are matched to the through-skull depth. Scale bar 50 μm . (b) Signal profile of a blood vessel in the deepest recorded vasculature fluorescence frame. The high SBR ratio implies that deeper imaging is possible using more energetic pulses.

A major advantage to three-photon imaging at 1700 nm wavelength is that red fluorescent proteins (RFPs), which have already been developed for conventional two-photon microscopy as well as calcium activity imaging, can also be excited with this technology. We used *Brainbow-1.0* line H mice [25] to perform through-skull imaging of cortical neurons. Figure 4.5 shows the 3D-rendered, RFP-labeled neuron stack. Details of the image processing are described in Methods. Neuronal imaging appears to be possible through Layer 2/3. Deeper imaging was hindered partially due to the lower neuron density below Layer 3.

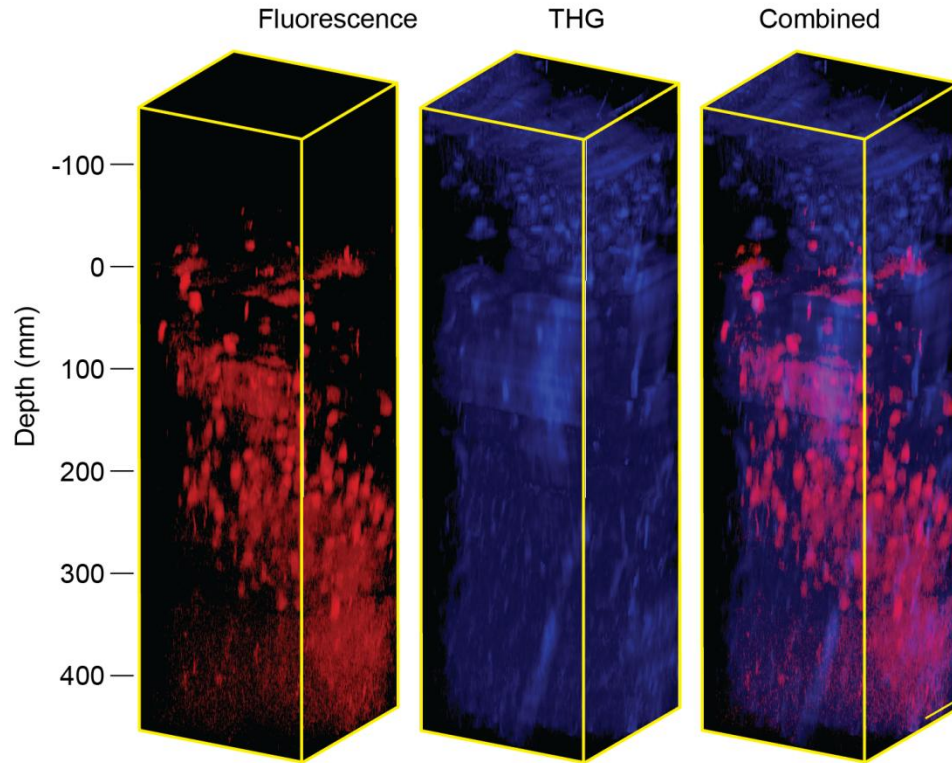


Figure 4.5: Three-dimensional rendering of RFP-labeled neurons in a mouse brain. The vasculature was not stained in this image, although THG imaging within the skull suggests the presence of a blood vessel. The scale bar is 50 μm .

Figure 4.6 shows individual frames from the *Brainbow-1.0* line H mouse experiment (Figure 4.5). Neurons are clearly visible 344 μm below the surface of the brain. Because neurons possess a large number of dendrites, the neuropil appears as a haze. This observation is similar to that shown in Horton 2013, which implies that the background brightness is not a factor for the through-skull imaging [17]. The large black circles in the frames below the surface are most likely blood vessels, which are not labeled. The decay curve is displayed in Fig. 4.8, and has similar properties to the curve in Fig. 4.3.

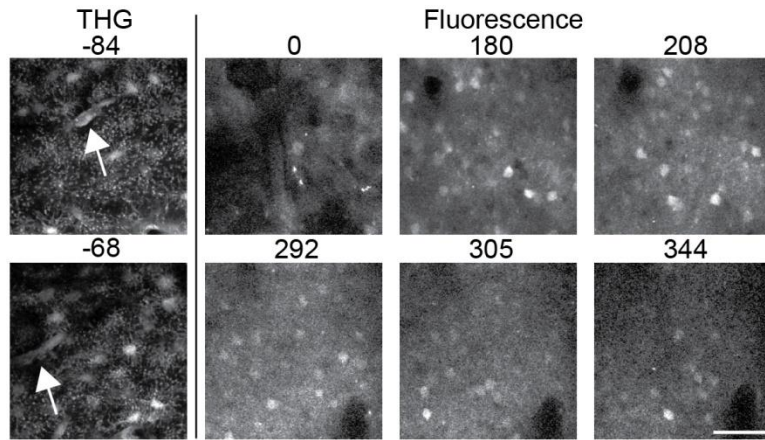


Figure 4.6: Frames from 8-week old RFP mouse. THG images show the signal generated in a skull, with the possible presence of vessels (arrows) Depths are relative to the skull-brain interface. Scale bar, 50 μm .

Figure 4.9 shows the through-skull lateral and axial resolution by plotting the fluorescence intensity distribution of an axon in an RFP-labeled mouse. The resolution is comparable to the craniotomy imaging in Horton [17]. For the axial resolution measurement, the signal generated by the surrounding neuropil increased as the signal approached the surface of the brain. Because of this, we fitted the data to a sloped Gaussian function.

4.4 Discussion

We produced the best through-skull imaging results when we made efforts to ensure the imaging region of the skull remained hydrated at all times. It was noticed that drying of the skull produced uneven patches of highly scattering skull material. When this was re-wetted, we noticed that the skull didn't possess the same translucency as before it was initially dried. Therefore, it is important to maintain skull moisture for the entire procedure.

The thickness of the mouse skull (100 to 130 μm) as indicated by the THG

signal is probably an under-estimated due to the high index of refraction of the skull ($n \sim 1.56$), which is approximately 20% higher than the index of water ($n \sim 1.33$). To corroborate the imaging result, we also measured the thickness of the *ex vivo* skull using a stereoscope (see Methods) to be approximately 150 μm at the imaging region, which is in rough agreement with published observations [14]. Differences in skull thickness also exist across different age of mice as well as different regions of the skull (the skull thickens near plate sutures), which may affect the maximum through-skull imaging depth within the brain.

Thermal damage is a concern for imaging above 1300 nm excitation, where water absorption becomes significant. We did not observe any thermal damage at 38 mW average power (500 kHz repetition rate), which is usually visible as a drop in signal after extended imaging deep within tissue.

Three-photon through-skull imaging with 1700 nm excitation is a valuable new tool for *in vivo* brain imaging, particularly for applications where minimum perturbation of the mouse brain is required. Limitations with the imaging depth are likely due to aberrations from the skull surface. Further advancements to the microscope, such as the introduction of adaptive optics for wavefront correction, may increase the resolution as well as the maximum imaging depth for this technology.

4.5 *Methods: imaging setup*

The microscope was prepared similar to that in Horton [17], with a few minor changes (Figure 4.7). We used an energetic femtosecond fiber laser that was capable of emitting 1.5 μJ of pulse energy at 1,550 nm wavelength. The laser was focused into

a Photonic Crystal (PC) rod with approximately $4600 \mu\text{m}^2$ effective mode-field area (A_{eff}). Soliton self-frequency shift within the PC rod generates an energetic soliton at $\sim 1700 \text{ nm}$. After the PC rod, the beam was filtered using both a 1630 nm long-pass filter and a 1030 nm long-pass filter. The power of the beam after the long-pass filters was 68 mW . The repetition rate could be set at 0.50 , 0.75 , 1.00 , or 1.33 MHz . We chose the repetition rate to be 0.5 MHz because this allowed us to maximize the pulse energy while still maintain low enough average power at the brain surface. Less than 40 mW average laser power were used under the objective lens, with which we did not notice any thermal damage to the tissue. A 3 mm Si wafer was added to the beam path, set at the Brewster angle relative to the input beam. This is to compensate the anomalous dispersion present in optical systems [26]. Both PMTs were GaAsP. A 593 nm LP filter (Semrock) was used for the fluorescence channel, and a $575/25 \text{ nm}$ bandpass filter was used for the THG channel. Each of these filters was placed at 18 degrees relative to incidence due to the collection pathway geometry in the Movable Objective Microscope (Sutter), which blue-shifted the frequency range to roughly 590 nm LP for the fluorescence channel and $568/18 \text{ nm}$ band-pass filter for the THG channel.

4.6 *Methods: mouse preparation*

We used male mice C57 for vasculature imaging and Brainbow1.0-HLich for RFP imaging. The C57 mouse presented was 10 weeks and the brainbow mouse was 8 & 12 weeks (for the depth imaging and resolution imaging, respectively). The mice were anesthetized using isoflurane. Hair was removed from the surgical site, and a circular region of the skin was removed using the scissors. Immediately after skin

removal, physiological saline (0.9%) was added to the opened site to ensure the skull remained moist. While the mouse skull is moist, the periosteum was removed using a cotton swab, and the skull was constantly moistened (the skull is prone to dry rapidly once the periosteum is removed, and the drying of the skull during any portion of the surgery can compromise the skull transparency). A 5 mm coverslip was placed on the skull, directly over the center of the parietal bone. Excess water around the skull was dried using cotton-tipped applicators. If the periosteum isn't entirely removed, it will be difficult to position the glass overhead. Cyanoacrylate glue is deposited around the perimeter of the coverslip to bond it to the skull. Once the cyanoacrylate dries, we dried the rest of the exposed skull area with 70% EtOH, then applied a layer of ferric chloride (until it dries), then a layer of cyanoacrylate. Once the cyanoacrylate dried, we place the metal stereotaxic bar on top of the mouse and added dental cement until we received a good contact. After the dental cement dried, we placed cyanoacrylate on the region to ensure a solid contact. We then took a polystyrene weighing dish (with a diameter larger than the diameter of the objective) and bonded it to a hole within a square plastic sheet (6" per side) using cyanoacrylate. We placed the dish on the mouse and made a seal with dental cement. After the cement dried, we added another layer of cyanoacrylate, which gave a hydrophobic surface. The mouse was then ready to image.

4.7 *Methods: imaging*

We chose an imaging region roughly 2 mm lateral and 2 mm caudal to bregma. We identified this region using white-light microscopy. The mouse platform was

affixed to the microscope by dropping two dowel pins through the mouse's stereotaxic platform and onto the microscope stage. This system allowed the removal and reinsertion of the mouse into the microscope with $\sim 25 \mu\text{m}$ precision. For our through-skull imaging experiment, dye (5% weight/volume Texas Red dextran-70,000, Life Technologies) was injected retro-orbitally into the mouse and the mouse was imaged through-skull under the microscope. For acquiring the post-craniotomy images of the same mouse, the mouse was removed from the setup, the craniotomy was performed according to Horton [17], and the mouse was returned to the microscope and the dowel pins were re-inserted between the platform and the microscope stage. Because the craniotomy removed the scattering and aberration-inducing skull, the signal was bright enough that an extra injection of dye wasn't necessary.

4.8 *Methods: image processing*

Images were collected using ScanImage. Post-processing procedures were identical to that in Horton [17].

The frames deeper than $380 \mu\text{m}$ in the C57 mouse and $150 \mu\text{m}$ in the brainbow mouse (below the skull-brain interface) were integrated for 5 frames, while shallower images were integrated for 2 frames. The deepest $100 \mu\text{m}$ of the vasculature-stained mouse were taken at a $10 \mu\text{m}$ interval (5 frames per depth), while all other frames were recorded at a $4 \mu\text{m}$ interval (800 nm step size for 5 frame averaging; $2 \mu\text{m}$ step size for 2 frame averaging). Integration time for each frame: $12.8 \mu\text{s}/\text{pixel}$, 512×512 pixels, 4s/frame. For the resolution measurement, single-frame integration was

performed at each measured depth. For all images, each frame was median-filtered (radius = 1 pixel) after integration.

A strong THG signal is produced within the mouse skull, which resulted in cross-channel leakage observed in the fluorescence channel. To compensate for cross-channel leakage, we normalized the fluorescence images to the THG channel within the skull, and we normalized the THG images to the fluorescence channel within the brain. If the THG signal was brighter than the fluorescence channel in the brain (e.g., the THG channel for brainbow imaging), we kept both channels at maximum normalization.

4.9 *Methods: skull thickness measurement*

The mouse was euthanized via isoflurane overdose, and a cervical dislocation was performed to confirm death. The calvarium was separated from the rest of the skull using surgical scissors, being careful not to damage the parietal bones. A surgical scissors was used to make a lateral cut across the calvarium, located 2 mm anterior to the bregma. This edge was mounted and positioned under a stereoscope, which was used to measure the skull thickness. The stereoscope was calibrated using a ruler, and readings were approximately 150 μm for C-57 mice. A caliper with 10 μm resolution was subsequently used to measure the skull thickness, which resulted in measurements ranging from 0.13-0.16 μm .

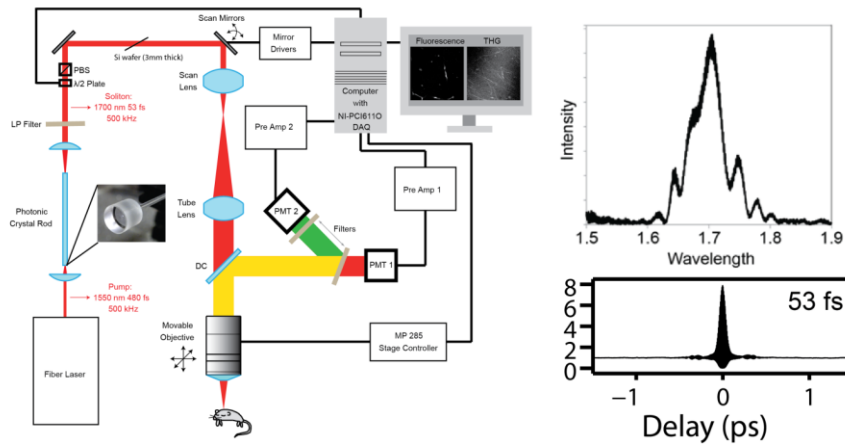


Figure 4.7: Left: Microscope setup. Right: The laser profile and second-order interferometric autocorrelation, assuming a sech^2 pulse. The FWHM of the intensity autocorrelation is also displayed.

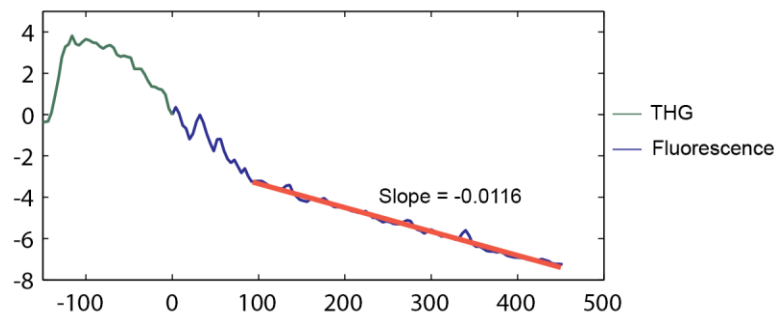


Figure 4.8: Signal decay curve of the RFP mouse. The green curve is THG within the skull, while the blue curve is fluorescence within the brain. The signal decay within the first 100 μm of the brain is roughly identical to that of the skull for each image, which is similar to our vasculature-stained mouse. The signal attenuation length deep within the brain (260 μm) also approximately matches the C57 data.

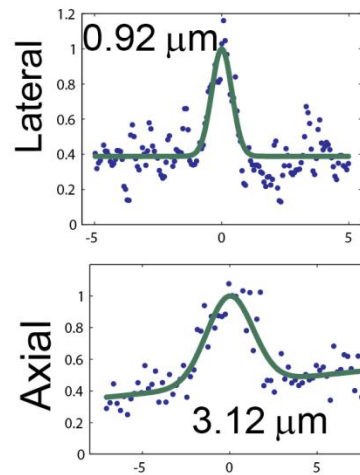
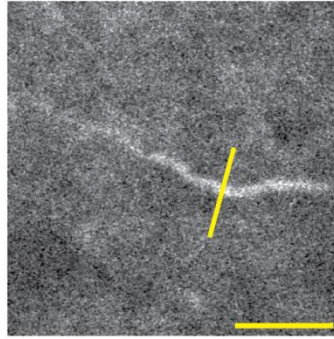


Figure 4.9: resolution tests of an RFP-labeled feature. This feature was located roughly 60 μm below the skull-brain interface.

REFERENCES

1. A. N. Van Den Pol and P. K. Ghosh, "Selective Neuronal Expression of Green Fluorescent Protein with Cytomegalovirus Promoter Reveals Entire Neuronal Arbor in Transgenic Mice," *J. Neurosci.* **18**, 10640-10651 (1998).
2. J. Chin, "Selecting a Mouse Model of Alzheimer's Disease," in *Alzheimer's Disease and Frontotemporal Dementia: Methods in Molecular Biology*, E. D. Roberson, ed. (2011), Vol. 670, pp. 169-189.
3. D. P. McCarthy, M. H. Richards, and S. D. Miller, "Mouse Models of Multiple Sclerosis : Experimental Autoimmune Encephalomyelitis and Theiler's Virus-Induced Demyelinating Disease," in *Autoimmunity: Methods and Protocols: methods in Molecular Biology*, A. Perl, ed. (2012), Vol. 900, pp. 381-401.
4. J. Blesa, S. Phani, V. Jackson-lewis, and S. Przedborski, "Classic and New Animal Models of Parkinson's Disease," *J. Biomed. Biotech.* **2012**, 845618 (2012).
5. H.-T. Xu, F. Pan, G. Yang, and W.-B. Gan, "Choice of cranial window type for in vivo imaging affects dendritic spine turnover in the cortex.," *Nat. Neurosci.* **10**, 549-51 (2007).
6. R. D. Dorand, D. S. Barkauskas, T. A. Evans, A. Petrosiute, and A. Y. Huang, "Comparison of intravital thinned skull and cranial window approaches to study CNS immunobiology in the mouse cortex," *IntraVital* **3**, e29728 (2014).
7. R. G. Pautler, "Mouse MRI : Concepts and Applications in Physiology," *Physiol.* **19**, 168-175 (2015).

8. X. Wang, Y. Pang, G. Ku, G. Stoica, and L. V. Wang, "Three-dimensional laser-induced photoacoustic tomography of mouse brain with the skin and skull intact," *Opt. Lett.* **28**, 1739-1741 (2003).
9. G. Hong, S. Diao, J. Chang, A. L. Antaris, C. Chen, B. Zhang, S. Zhao, D. N. Atochin, P. L. Huang, K. I. Andreasson, C. J. Kuo, and H. Dai, "Through-skull fluorescence imaging of the brain in a new near-infrared window," *Nat. Photon.* **8**, 723-730 (2014).
10. C. Stosiek, O. Garaschuk, K. Holthoff, and A. Konnerth, "In vivo two-photon calcium imaging of neuronal networks.," *PNAS* **100**, 7319-24 (2003).
11. Y. Jia and R. K. Wang, "Optical micro-angiography images structural and functional cerebral blood perfusion in mice with cranium left intact," *J. Biophoton.* **4**, 57-63 (2011).
12. R. K. Wang, S. L. Jacques, Z. Ma, S. Hurst, S. R. Hanson, and A. Gruber, "Three dimensional optical angiography," *Opt. Exp.* **15**, (2007).
13. P. A. Murphy, T. N. Kim, G. Lu, A. W. Bollen, C. B. Schaffer, and R. A. Wang, "Notch4 normalization reduces blood vessel size in arteriovenous malformations.," *Sci. Translat. Med.* **4**, 117ra8 (2012).
14. L. Kong and M. Cui, "In vivo fluorescence microscopy via iterative multi-photon adaptive compensation technique," *Opt. Exp.* **22**, 23786-23794 (2014).
15. W. Denk, J. H. Strickler, and W. W. Webb, "Two-photon laser scanning fluorescence microscopy," *Science* **248**, 73-76 (1990).
16. D. Kobat, N. G. Horton, and C. Xu, "In vivo two-photon microscopy to 1.6-mm depth in mouse cortex.," *J. Biomed. Opt.* **16**, 106014 (2011).

17. N. G. Horton, K. Wang, D. Kobat, C. G. Clark, F. W. Wise, C. B. Schaffer, and C. Xu, "In vivo three-photon microscopy of subcortical structures within an intact mouse brain," *Nat. Photon.* **7**, 205-209 (2013).
18. I. A. Bab, C. Hajbi-Yonissi, Y. Gabet, and R. Mueller, *Micro-tomographic Atlas of the Mouse Skeleton* (Springer, 2007).
19. A. Ascenzi and C. Fabry, "Technique for Dissection and Measurement of Refractive Index of Osteones," *J. Biophys. Chem.* **6**, 139-142 (1959).
20. A. Vatsa, R. G. Breuls, C. M. Semeins, P. L. Salmon, T. H. Smit, and J. Klein-Nulend, "Osteocyte morphology in fibula and calvaria – Is there a role for mechanosensing?," *Bone* **43**, 452-458 (2008).
21. C. Lo Celso, H. E. Fleming, J. W. Wu, C. X. Zhao, S. Miake-Lye, J. Fujisaki, D. Côté, D. W. Rowe, C. P. Lin, and D. T. Scadden, "Live-animal tracking of individual haematopoietic stem/progenitor cells in their niche.," *Nature* **457**, 92-96 (2009).
22. L. A. Moulopoulos and V. Koutoulidis, *Bone Marrow MRI: A Pattern-Based Approach* (Springer, 2015).
23. D. Débarre, N. Olivier, and E. Beaupaire, "Signal epidetection in third-harmonic generation microscopy of turbid media.," *Opt. Exp.* **15**, 8913-8924 (2007).
24. E. A. Genina, A. N. Bashkatov, and V. V. Tuchin, "Optical Clearing of Cranial Bone," *Adv. Optic. Technol.* **2008**, 267867 (2008).
25. J. Livet, T. A. Weissman, H. Kang, R. W. Draft, J. Lu, R. A. Bennis, J. R. Sanes, and J. W. Lichtman, "Transgenic strategies for combinatorial

expression of fluorescent proteins in the nervous system,” *Nature* **450**, 56-62 (2007).

26. N. G. Horton and C. Xu, “Dispersion compensation in three-photon fluorescence microscopy at 1,700 nm,” *Biomed. Opt. Exp.* **6**, 1392-1397 (2015).

CHAPTER 5

FUTURE EXPERIMENTS

5.1 *Introduction*

Chapters 2-4 describe 3PM at 1700 nm excitation wavelength and demonstrate its ability to image significantly deeper *in vivo* than shorter-wavelength 2PM. This advancement permits new imaging opportunities deeper within the brain and other tissues. This chapter briefly discusses 1700 nm 3PM limitations due to thermal heating, new applications for *in vivo* mouse imaging, and applications for *in vivo* human imaging.

5.2 *Thermal heating considerations*

Thermal heating during deep-imaging experiments, due to water absorption near the tissue surface, can irreversibly alter the tissue structure. This limits the average power that can be incident on the sample surface. For example, when imaging 1.0 mm below the surface of the brain with 70 mW average power at 1700 nm, an initially bright signal dims drastically over a ~10s period, which implies that tissue heating decreased the attenuation length of overlying tissue. However, we do not notice any reduction in signal when the average power was below approximately 55 mW. Since 3PM signal generation is proportional to the cube of the average power and the inverse-square of the duty cycle [1], a low repetition rate is preferred over attenuated pulse energies for systems limited by tissue heating. Because of this, although our current laser system is capable of a 1.3 MHz repetition rate, we set it to

500 kHz, which corresponds to 68 mW power after the longpass filters and 38 mW after the microscope objective. Larger-area PC rods will allow solitons with even higher pulse energies and therefore even higher signal generation within the brain, with the potential to image the *dentate gyrus* of the hippocampus. However, this potential factor-of-two increase in the soliton energy will require a ~250 kHz laser repetition rate for imaging. Because of this lower repetition rate, great care must be taken to ensure that an adequate number of pulses are integrated at each pixel. To achieve this, either the laser pulses must be synchronized to the computer [2] or the scan mirrors must perform a nonuniform scan pattern [3], which will allow longer pulse integration per pixel by only scanning over important regions in the image. It is important to note that ScanImage [4], a popular laser scanning microscope system, currently does not support pulse synchronization.

5.3 *New applications for mouse imaging*

Two applications for mouse imaging that can benefit from 1700 nm 3PM are described below.

1) Fast mapping of the brain.

Whole-brain fluorescence scanning at high-resolution is critical for mapping the brain's neural network within a reasonable time. Recent advancements in optical tissue clearing allow rapid three-dimensional fluorescence imaging of *ex vivo* brain tissue using light-sheet microscopy [5].

During our *in vivo* imaging experiments, we observe that vasculature and neural bodies deep within the brain can be roughly identified using one-or two-

frame integration. Since these fluorescent structures tend to be ~10% of the field of view, a nonuniform scan pattern can be used to provide long-integration-time imaging at relevant tissue areas [3,6,7]. In order to accomplish this, a 512x512 pixel scan can be performed, and regions that are likely to contain features can be identified. After these features are identified, they can be selectively imaged with longer integration times.

2) Imaging *real-time* neural communication

Fast scanning is especially critical if neural firing is to be imaged *in vivo*. Neural activity is commonly imaged using calcium-sensitive dyes [8], which operate with roughly > 200 ms temporal resolution. Therefore, scanning rates as low as 50 Hz can provide sufficient imaging of these calcium transients. One-dimensional line scanning of the laser across a neuron will allow spiking to be visualized even when the entire neuron isn't resolved, and an arbitrary scan pattern can be generated with nonresonant scan mirrors to rapidly observe multiple neurons within in a field of view. Neurons have been imaged using lasers with as low as 200 kHz pulse repetition rates [9]. Red fluorescent calcium indicators are necessary for three-photon microscopy at 1700 nm excitation, and recent progress has been made to develop brighter calcium-sensitive red fluorescent proteins for *in vivo* imaging with high resolution. *In vivo* calcium imaging can be efficiently performed if a slow scan is first made across the field of view to identify neuron locations, which is then followed by a faster line scan or arbitrary scan pattern for calcium imaging across the desired neurons.

5.4 *Deep-Tissue THG imaging*

THG microscopy was previously shown useful for identifying myelin sheaths surrounding axons [10,11]. Deep-tissue THG has also been shown useful for guiding pipettes into proper injection sites [12], and even for imaging red blood cells in human skin *in vivo* [13]. Improvements with 3PM will permit each of these applications deeper within tissue.

5.5 *In vivo human tissue imaging*

MPM for *in vivo* human tissue imaging is currently more limited than animal imaging due to regulatory concerns. A commercial MPM system called Dermaininspect was recently developed for skin analysis in Europe, Asia, and Australia [14], and further testing could result in MPM imaging technologies for human use in the United States.

THG has significant advantages over fluorescence in human imaging because it doesn't rely on fluorescent dyes. THG has already been shown to image human red blood cells *in vivo* [13] and has been hypothesized to provide bright contrast for nerve imaging. Nerves are especially difficult to identify using white-light microscopy, which limits the ability of surgeons to avoid severing them.

MPM fluorescence microscopy can potentially have a tremendous application for *in vivo* cancer detection in humans, and the ability to easily detect cancer margins will drastically increase cancer survival rates. Although autofluorescence of intrinsic molecules is commonly used in 2PM at shorter wavelengths [15], 1700 nm 3PM does not appear to excite intrinsic autofluorescence. The lack of autofluorescence could be

beneficial in the sense that only introduced contrast agents will produce a fluorescent signal.

Miniaturized probes for MPM are also possible for 1700 nm 3PM. A 2PM endoscope was recently demonstrated by Rivera *et al.* [16], which was used to image autofluorescence. In addition, Huland *et al.* demonstrated three-photon autofluorescence imaging at 1040 nm using a rigid endoscope with a gradient-index (GRIN) lens [17]. Both of these techniques can be designed for 1700 nm 3PM but would likely require different optical coatings.

5.6 Conclusion

MPM revolutionized deep tissue *in vivo* imaging when it was first introduced in 1990, and 1700 nm 3PM provides a significant improvement in penetration depth over previous systems. Future advancements with brighter dyes and fluorescent proteins will allow even deeper imaging within tissue, which will lead to newer applications for both basic research and medicine.

REFERENCES

1. Xu, C. & Webb, W. W. Multiphoton excitation of molecular fluorophores and nonlinear laser microscopy, *In Topics in fluorescence spectroscopy*, Vol. 5 (Ed, Lakowicz, J. R.), 471-540.
2. P. Theer, M. T. Hasan, and W. Denk, "Two-photon imaging to a depth of 1000 microm in living brains by use of a Ti:Al₂O₃ regenerative amplifier," *Opt. Lett.* **28**, 1022-1024 (2003).
3. G. Katona, G. Szalay, P. Maák, A. Kaszás, M. Veress, D. Hillier, B. Chiovini, E. S. Vizi, B. Roska, and B. Rózsa, "Fast two-photon in vivo imaging with three-dimensional random-access scanning in large tissue volumes," *Nat. Method.* **9**, 201-208 (2012).
4. T. A. Pologruto, B. L. Sabatini, and K. Svoboda, "ScanImage: flexible software for operating laser scanning microscopes," *Biomed. Eng. OnLine* **2**, 13 (2003).
5. R. Tomer, L. Ye, B. Hsueh, and K. Deisseroth, "Advanced CLARITY for rapid and high-resolution imaging of intact tissues," *Nat. Prot.* **9**, 1682-1697 (2014).
6. R. Salome, Y. Kremer, S. Dieudonne, J. F. Leger, O. Krichevsky, C. Wyart, D. Chatenay, and L. Bourdieu, "Ultrafast random-access scanning in two-photon microscopy using acousto-optic deflectors," *J. Neurosci. Method.* **154**, 161-174 (2006).
7. G. D. Reddy and P. Saggau, "Random-Access Multiphoton Microscopy for Fast Three-Dimensional Imaging," *In Membrane Potential Imaging in the*

- Nervous System: Methods and Applications*, (Eds, M. Canepari and D. Zecevic) 139-145 (2010).
8. C. Grienberger and A. Konnerth, "Imaging Calcium in Neurons," *Neuron* **73**, 862-885 (2012).
 9. W. Mittmann, D. J. Wallace, U. Czubayko, J. T. Herb, A. T. Schaefer, L. L. Looger, W. Denk, and J. N. D. Kerr, "Two-photon calcium imaging of evoked activity from L5 somatosensory neurons in vivo.," *Nat. Neurosci.* **14**, 1089-1093 (2011).
 10. M. J. Farrar, F. W. Wise, J. R. Fetcho, and C. B. Schaffer, "In vivo imaging of myelin in the vertebrate central nervous system using third harmonic generation microscopy," *Biophys. J.* **100**, 1362-1371 (2011).
 11. N. G. Horton, K. Wang, D. Kobat, C. G. Clark, F. W. Wise, C. B. Schaffer, and C. Xu, "In vivo three-photon microscopy of subcortical structures within an intact mouse brain," *Nat. Photon.* **7**, 205-209 (2013).
 12. S. Witte, A. Negrean, J. C. Lodder, C. P. J. de Kock, G. T. Silva, H. D. Mansvelder, and M. L. Groot, "Label-free live brain imaging and targeted patching with third-harmonic generation microscopy," *PNAS* **108**, 5970-5975 (2011).
 13. C.-K. Chen and T.-M. Liu, "Imaging morphodynamics of human blood cells in vivo with video-rate third harmonic generation microscopy.," *Biomed. Opt. Exp.* **3**, 2860-2865 (2012).
 14. K. Konig, "Clinical multiphoton tomography," *J. Biophoton.* **1**, 13-23 (2008).

15. W. R. Zipfel, R. M. Williams, R. Christie, A. Y. Nikitin, B. T. Hyman, and W. W. Webb, "Live tissue intrinsic emission microscopy using multiphoton-excited native fluorescence and second harmonic generation.," *PNAS* **100**, 7075-7080 (2003).
16. D. R. Rivera, C. M. Brown, D. G. Ouzounov, I. Pavlova, D. Kobat, W. W. Webb, and C. Xu, "Compact and flexible raster scanning multiphoton endoscope capable of imaging unstained tissue," *PNAS* **108**, 17598-17603 (2011).
17. D. M. Huland, K. Charan, D. G. Ouzounov, J. S. Jones, N. Nishimura, and C. Xu, "Three-photon excited fluorescence imaging of unstained tissue using a GRIN lens endoscope," *Biomed. Opt. Exp.* **4**, 652-658 (2013).